Plasma exosomes from individuals with type 2 diabetes drive breast cancer aggression in patient-derived organoids

Christina S. Ennis[1], Michael Seen[1], Andrew Chen[2,3], Heejoo Kang[1], Adrian Ilinski[4], Kiana Mahdaviani[4], Naomi Ko[4], Stefano Monti[2,3,5], Gerald V. Denis[1,4,6]

[1]Cancer Center, Boston University Chobanian and Avedisian School of Medicine, Boston, Massachusetts, USA

[2]Department of Medicine, Computational Biomedicine Section, Boston University Chobanian and Avedisian School of Medicine, Boston, Massachusetts, USA

[3]Bioinformatics Program, Faculty in Computing and Data Science, Boston University, Boston, Massachusetts, USA

[4]Section of Hematology/Oncology, Department of Medicine, Boston University Chobanian and Avedisian School of Medicine, Boston, Massachusetts, USA

[5]Department of Biostatistics, Boston University School of Public Health, Boston, Massachusetts, USA

[6]Department of Pharmacology and Experimental Therapeutics, Boston University Chobanian and Avedisian School of Medicine, Boston, Massachusetts, USA

Keywords. Breast cancer, patient-derived organoids, exosome, cancer immunology, tumor niche dynamics

Grant Support. This work was supported by grants from NIH: U01CA182898, U01CA243004 and R01CA222170 to G.V. Denis; 5T32AI007309 (PI: Gummurulu) to C.S. Ennis.

Corresponding Author. Gerald V Denis, Boston University Chobanian and Avedisian School of Medicine School of Medicine, 72 East Concord Street, Rm K408, Boston, MA 02118 Phone: 617-414-1371, Lab: 617-414-1372, Fax 617-638-5673; E-mail: gdenis@bu.edu

Conflict of interest. The authors affirm that they have no conflicts to disclose.

Word count, excluding references: 3916

Figures: 6

References: 70

Abstract

Women with obesity-driven diabetes are predisposed to more aggressive breast cancers. However, patient metabolic status does not fully inform the current standard of care. We previously identified plasma exosomes as functionally critical actors in intercellular communication and drivers of tumor progression. Here, we generated patient-derived organoids (PDOs) from breast tumor resections to model signaling within the tumor microenvironment (TME). Novel techniques and a short (1-week) culture preserved native tumor-infiltrating lymphocytes for the first time in breast tumor PDOs. After 3-day exosome treatment, we measured the impact of exosomal signaling on PDOs via single-cell RNA sequencing. Exosomes derived from Type 2 diabetic patient plasma significantly upregulated pathways associated with epithelial-to-mesenchymal transition, invasiveness, and cancer stemness, compared to non-diabetic exosome controls. Intratumoral heterogeneity and immune evasion increased in the diabetic context, consistent with enhanced tumor aggressiveness and metastatic potential of these PDOs. Our model of systemic metabolic dysregulation and perturbed transcriptional networks enhances understanding of dynamic interactions within the TME in obesity-driven diabetes and offers new insights into novel exosomal communication.

(169 words)

Metabolic disorders, particularly Type 2 diabetes (T2D), raise concerns for the management of breast cancer. Population studies have shown that women with T2D have 40% increased risk of developing breast cancer and 74% increase in overall mortality compared to non-diabetic (ND) women[1]. The alarming impact of this comorbidity underscores a critical gap in our understanding of the cellular and molecular mechanisms linking these diseases. Recently, investigations into the immune phenotype of T2D have described subclinical chronic inflammation that induces insulin resistance and metabolic dysfunction that accompany the disease[2,3]. This inflammatory milieu ultimately leads to T cell dysfunction[4], posing a significant clinical challenge for breast cancer patients. Cancer cells have adaptations that allow them to exploit this dysfunction, reprogramming immune cells to evade detection and clearance[5]. Traditional molecular diagnostics fall short in capturing these profound differences seen in the tumor microenvironment (TME) of T2D[1], highlighting an urgent need for improved diagnostic and therapeutic approaches. Here, we use novel models to focus on unique features of this TME to explore mechanisms that may contribute significantly to breast cancer progression in T2D.

Within the breast TME, exosomes have emerged as key mediators of cellular communication. Initially dismissed as mere cellular disposal systems, these nano-sized extracellular vesicles are now recognized for their crucial roles in transferring bioactive molecules, such as proteins, lipids, and nucleic acids, between cells that influence tumor behavior and progression[6,7]. Our group and others have recently highlighted the critical role of exosomes in linking metabolic dysregulation with cancer pathophysiology[7–9]. We demonstrated that exosomes isolated from T2D patient adipocytes promote a more aggressive tumor phenotype in cellular models of breast cancer, increasing epithelial-to-mesenchymal transition (EMT) and cancer stem-like cell (CSC) formation, compared to ND controls[10]. Similarly, plasma-derived exosomes from T2D patients enhanced EMT and CSC traits in prostate cancer cell lines[11]. Furthermore, T2D exosomes carry distinctive biomarkers that could serve as diagnostic or prognostic tools[7,11], and offer new insights into the intercellular communication of the TME that drives breast cancer progression in

metabolic disorders. However, these studies have yet to fully elucidate how exosomal treatment affects other cell types of the TME, and how this might exacerbate overall tumor aggressiveness.

Accurate modeling of the TME presents a challenge due to its intricate and dynamic cellular interactions. Recent advances in three-dimensional *in vitro* systems, such as patient-derived organoids (PDOs), have started to bridge this gap by preserving the heterogeneity and architecture of the originating tumors[12,13]. Leveraging this model, coupled with advancements in single-cell RNA sequencing - although sparingly used in breast cancer PDO research - have been instrumental in uncovering critical molecular pathways involved in drug response and detailing the landscape of intratumoral heterogeneity preserved in PDOs[14,15]. However, a significant limitation has been the attrition and eventual elimination of the immune fraction[16,17]. Our novel approach enhances standard breast cancer PDO models by successfully preserving and comprehensively profiling native, primary breast tumor-infiltrating lymphocytes (TILs). This advancement is a significant stride in breast cancer research, as it allows for a more accurate study of the immune-tumor interactions within the TME.

Here, we explore how exosomes derived from T2D patient plasma increase the aggressiveness of breast cancer. We hypothesize that T2D plasma-derived exosomes promote oncogenic processes, including EMT, CSC formation, and immune evasion, within the PDO model. Elucidating these interactions will refine our understanding of the role of T2D in breast cancer progression, offering novel insights that could fundamentally alter clinical approaches to breast cancer treatment.

Results

Single-cell RNA sequencing reveals cellular landscape of PDOs

To elucidate the cellular architecture and explore the effects of exosomal communication in breast cancer, we developed a robust *in vitro* model using PDOs generated from ER+ breast tumor resection samples from three ND patients (Fig. 1a, Table S1). Briefly, tumor tissues were mechanically and

enzymatically digested with collagenase, and the resulting cell clusters were embedded in a basement membrane extract (BME) and cultured with a cocktail of growth factors to support organoid formation and maintain native TME populations. PDOs were then treated with plasma-derived exosomes from two carefully selected patients to minimize experimental variability: an ND individual (ND*exo*-PDOs) and a patient with T2D (T2D*exo*-PDOs, glycated hemoglobin (HbA1c) 9.3%). These donors were chosen based on a preliminary screen of 15 patients, selecting those that would maximize the detection of functional differences in TME behavior. This approach ensured consistent experimental conditions across different PDO batches and facilitated a focused examination of how metabolic status influences TME dynamics. Plasma exosomes were isolated from EDTA-anticoagulated, peripheral venous blood, and quantified to deliver 5,000 particles per PDO cell. A control group of untreated PDOs (UT-PDOs) was maintained to establish a baseline for comparison.

After stringent quality control (see Methods), we obtained transcriptomes of 24,599 single cells across three independently generated PDO lines each under three conditions, UT, ND*exo*, and T2D*exo* subjected to exosome treatment (Fig. 1b-d, 318: UT - n = 2007, ND*exo* - n = 2384, T2D*exo* - n = 2562; 377: UT - n = 5396, ND*exo* - n = 6915, T2D*exo* - n = 4953; 409: UT - n = 164, ND*exo* - n = 124, T2D*exo* - n = 94). The samples were integrated computationally using single-cell variational inference (scVI)[18,19] to address interpatient variability of tumor cell fractions (Fig. S1a,b). Copy number alterations were used to distinguish neoplastic from normal cells, leveraging immune cells also captured within PDOs (Fig. 1e, Fig. S2a-c). Tumor cell identities were validated by comparing gene expression profiles of breast cancer-specific gene sets from the Catalogue of Somatic Mutations in Cancer (COSMIC) Cancer Gene Census (CGC)[20] and gene sets related to mammary epithelial proliferation[21] (Fig. S1d).

Unsupervised uniform manifold approximation and projection (UMAP)-clustering revealed 17 clusters, which were further classified via automatic cell annotation[22,23] and established lineage-specific marker genes (Fig. 1f, Fig. S1e, Table S2). Notably, many crucial cell types were abundantly present

across all patient samples (Fig. 1c). We identified 20,173 epithelial cells, which accounted for the majority of sequenced cells. We identified three major stromal cell types (Fig. 1b) including cancer associated fibroblasts (CAFS; *FAP, COL1A1*), perivascular-like cells (PVL; *PDGFRA, PDGFRB*), and endothelial cells (*PECAM1, CD34*). Critically, we identified distinct clusters relating to various immune cell types, including T cells (*CD3E, CD8A*), B cells (*MS4A1, PAX5*), and macrophages (*CD68, CD163*). This achievement marks a significant advance over traditional breast cancer PDO methods, which commonly fail to maintain native breast TIL populations, thereby underscoring the fidelity of our model to recapitulate the *in vivo* TME and its immune landscape.

T2D*exo*-PDOs exhibit aggressive phenotypes, compared to ND*exo*-PDOs

To elucidate the distinct transcriptional impacts of T2D-exosomal communication, we conducted gene set enrichment analysis (GSEA)[24,25] on differentially expressed genes across all cell populations (Table S3). All changes we report were statistically significant. T2D*exo*-PDOs showed upregulation of pathways related to EMT, invasiveness, and stemness (Fig. 2a,b). These hallmark processes are associated with aggressive tumor phenotypes and metastatic potential, consistent with our previous findings that T2D exosomes upregulate such pathways in breast cancer models[10,26]. These findings were further validated by examining the expression of breast cancer genes listed in the COSMIC CGC and canonical CSC markers as shown previously[10], both of which were upregulated in the T2D*exo* epithelial cell fraction compared to ND*exo*-PDOs (Fig. 2c). Furthermore, the top differentially expressed genes include well known drivers of aggressiveness and stemness (Fig. 2d, Table S4; *NOTCH1, MMP14*). These results align with our prior PCR-validated data[10], strengthening the evidence that T2D exosomes promote aggressive cancer phenotypes. Morphological assessments of PDOs supported these findings, with T2D*exo*-PDOs displaying pronounced budding (Fig. 2e,f, Table S5), a morphological indicator of increased metastatic capacity[27,28]. Such findings are consistent with our previous reports of T2D exosomes promoting

migration and morphological changes in other cellular models[10,11,29], further reinforcing their role in enhancing tumor aggressiveness. Conversely, ND*exo*-PDOs demonstrated activation of T cell mediated immune responses (Fig. 2a,c,d, Table S3). Specifically, pathways related to antigen binding and presentation, along with cytotoxic T cell signaling, were upregulated in ND*exo* relative to T2D*exo*-PDOs, indicating enhanced tumor immunogenicity and immune system recognition.

Exosomes from T2D plasma increase intratumoral heterogeneity

Given the predominance of epithelial cells in our dataset, we next analyzed epithelial lineage-specific responses within T2D*exo*-PDOs versus ND*exo*-PDOs. We identified 11 distinct cell clusters (Fig. 3a,b, Table S6), representing typical epithelial cell types, including normal luminal epithelial (LEC; *KRT18*), myoepithelial (MEC; *TAGLN, KRT14*), and cycling cells (CYC; *MKI67, TOP2A*).

Malignant cells were further classified into two distinct groups: luminal-like and basal-like. The luminal-like group consisted of five clusters (LT1-5), defined by *ESR1* positivity and expression of *KRT19*, whereas the basal-like group comprised two clusters (BT1-2) characterized by *ESR1* negativity and expression of canonical basal markers (*KRT5, VIM*). Despite all patients being clinically diagnosed as ER-positive, our data, consistent with other studies[23], highlighted subtype mixing within individual tumors that was faithfully recapitulated in PDOs. In addition to these clearly malignant clusters, we identified a population of luminal progenitor-like cells (LP; *KIT, ELF5*), which are considered the presumptive cells of origin for breast cancer and are indicative of cancer stemness[30].

In the luminal-like group, we identified five subtypes (Table S6). Clusters LT1 and LT2 showed high expression of genes associated with energy metabolism and oxidative stress (*MALAT1, NDUFC2, ELOB*). LT3 exhibited a heightened proliferation index, indicated by increased expression of *MKI67* and *TOP2A*, and genes marking breast epithelium (*ANKRD30A*). LT4 was characterized by genes linked to increased immune infiltration (*HLA-A, B2M*). LT5 showed upregulation of genes associated with poor

clinical outcomes (*MUC1, SERPINA3*). Within the basal-like fraction, most cells belonged to the BT1 cluster, marked by the expression of hallmark aggressive genes (*VIM, ITGA6*). Conversely, BT2 was characterized by genes associated with a protein synthesis phenotype (*RPS15*).

To probe how exosome treatment impacted luminal-like tumor cell niches, we conducted a differential proportion analysis of tumor clusters. We observed expansion of the LT1 cluster, coupled with contraction of LT3 in T2D*exo* compared to ND*exo*-PDOs (Fig. 3c, Fig. S3a,b). GSEA of the LT1 marker genes revealed upregulation of oncomiR targets (Fig. 3d, Fig. S3c, Table S7) suggesting functional activity of the specific miRNAs delivered by T2D-derived exosomes as previously reported[11,29]. This aligns with studies showing that oncomiRs target matrix metalloproteinase (MMP) regulators[31], triggering MMP upregulation as observed in this cluster (*MMP24OS*). Notably, we observed upregulation of genes targeted by miR-374a, aligning with our earlier findings that miR-374a levels are elevated in T2D plasma exosome cargo compared to ND-plasma exosomes[11]. These findings suggest a network or systems-level approach in understanding miRNA-mediated regulation, rather than focusing on individual miRNAs.

Exosome treatment accelerates tumor cell evolution

To examine the evolutionary shifts induced by exosome treatment, we performed pseudotime analysis[32] on the luminal-like epithelial cell fraction in PDOs, excluding basal-like epithelial, immune, stromal, and cycling populations. Ordering these cells in pseudotime revealed a principal trajectory from normal LECs to more transformed states. Notably, cells from T2D*exo*-PDOs were positioned significantly later in pseudotime compared to those from ND*exo* or UT-PDOs (Fig. 4a), indicating that T2D plasma-derived exosomes promote substantial evolution in tumor cell phenotypes. Overlaying tumor subclones onto the pseudotime trajectory (Fig. S4a) revealed that the LT1 subclone was positioned furthest along in pseudotime. This finding correlates with a higher proportion of LT1 cells in T2D*exo*-PDOs, potentially explaining their advanced pseudotime positioning.

To delineate the specific evolutionary paths captured by pseudotime, we performed differential gene expression using graph-autocorrelation. All changes we report were statistically significant. This analysis revealed upregulation of oncogenic genes (Table S8; *MKI67, MMP2, PTMA*) along the trajectory (Fig. 4b). Conversely, major histocompatibility complex (MHC) class I molecules (*HLA-A, HLA-B, HLA-C*) were progressively downregulated, a common immune evasive strategy by cancer cells to thwart immune detection and clearance[33]. Grouping these differentially expressed genes into co-regulated modules resulted in eight distinct clusters (Fig. 4c). Importantly, module 5, which showed an increased expression through pseudotime (Fig. S4b,c, Table S9), was upregulated in T2D*exo*-PDOs compared to ND*exo* or UT-PDOs (Fig. 4d). Functional enrichment analysis using the Database for Annotation, Visualization, and Integrated Discovery (DAVID) resource[34,35] revealed that this module is involved in EMT (*CTNNB1, TRIM28, BRD2*), RNA splicing (*SNRNP70, SRSF4*), and aerobic metabolism (*ATP5F1A, MT-ND5*) which are well known to be perturbed in T2D [1,36]. These findings are consistent with our previous reports where treatment of MCF7 cells with T2D-derived exosomes induced shifts in metabolic pathways[10].

T2D*exo*-PDOs display enhanced immune evasion through T cell dysfunction

Given the significant downregulation of T cell signaling, we conducted a focused analysis of the immune cell compartment within T2D*exo*-PDOs compared to ND*exo*-PDOs. We identified 10 distinct cell clusters representing 1,760 various immune cells (Fig. 5a,b, Table S10) upon reclustering, including T cells (*CD3E, TRAC)*, B cells (*MS4A1, CD79A*), plasma cells (*MZB1, SDC1*), and macrophages (*CD68, CD163*).

T cells were further classified into six distinct subsets. The largest proportion consisted of memory T cells, including central memory (Tcm; *SELL, CCR7*) and effector memory T cells (Tem; *SELL-, CCR7-*). We also identified clear populations of active anti-tumorigenic T cell states, including effector T (Teff;

CD8A, GZMB) and T helper 1 cells (Th1; *CD4, IFNG*). We also found a notable population of mucosal-associated invariant T cells (MAIT; *KLRB1, IL18R1*), an unconventional subset recognized for their innate-like effector functions and potential importance in antitumor immunity[37]. In addition to these well-defined T cell subsets, we identified a conserved cluster (ChopT) characterized by the expression of *DDIT3*, which encodes the transcription factor CHOP (Fig. S5a-c). CHOP is a downstream sensor of severe endoplasmic reticulum (ER) stress, and acts as a major negative regulator of both CD8+ and CD4+ T cell effector function[38,39].

We next explored how exosome treatment alters native TIL function by performing differential cell proportion analysis (Table S11). We saw expansion of ChopT cells, coupled with contraction of Tcm and MAIT (Fig. 5c). Further, GSEA analysis restricted to immune cells highlighted enhanced anti-inflammatory signaling via interleukin-10 (IL-10) and decreased proinflammatory signaling via the tumor necrosis factor (TNF) superfamily (Fig. 5d, Fig. S5d, Table S12)[40,41]. We also identified gene sets related to hypoxia and defective metabolism. Additionally, GSEA revealed upregulation of cytotoxic and effector responses, including antigen binding and T cell receptor (TCR) signaling, in ND*exo*-PDOs (Fig. 5d). Collectively, these data demonstrate a clear and distinct profile of immune evasion in T2D*exo* compared to ND*exo*-PDOs.

Exosomes modulate intercellular communication in T2D*exo*-PDOs

To further characterize the immune evasive TME of T2D*exo*-PDOs compared to ND*exo*-PDOs, we performed ligand-receptor interaction analysis[42,43] between all identified cell types (Fig. 6a-d, Fig. S6a,b). Overall, 95 pathways relating to 1142 genes were involved in building the communication network, including 69 conserved pathways, 10 ND*exo*-specific and 16 T2D*exo*-specific pathways (Fig. 6e, Fig. S6c,d, Table S13). This analysis revealed upregulated NOTCH (e.g., JAG1 - NOTCH1) and bone morphogenic protein (BMP; e.g., BMP7 - [BMPR1B+BMPR2]) signaling in T2D*exo*-PDOs, promoting

stem-like characteristics and resistance to apoptosis[44,45]. These findings are supported by our previous work, where we consistently observed downregulation of apoptosis in T2D exosome-treated models[10,29]. Additionally, T2D*exo*-PDOs exhibited enhanced extracellular matrix remodeling with heightened interactions involving MMPs (e.g., MMP2 - ([TGAV+ITGB3]) crucial for tumor cell invasion and migration[46]. Further, T2D*exo*-PDOs showed increased TNF-related apoptosis-inducing ligand (TRAIL) signaling (e.g., TNFSF10 - TNFRSF10B), which has been linked to immunosuppression within the TME[47]. Conversely, ND*exo*-PDOs displayed upregulated communication involving MHC class-I, MHC class-II, and CXCL signaling, indicative of a more robust antitumor immune response[33,48]. All changes we report were statistically significant.

We observed a dense communication network in T2D*exo*-PDOs among basal-like tumor cells and CAFs with all other annotated cell types (Fig. 6f). Focusing specifically on differential T cell ligand-receptor interactions, T2D*exo*-PDOs demonstrated distinct signaling alterations, notably in the thrombospondin pathway (Fig. 6g, Fig. S7a,b). This pathway is well known for its immunosuppressive action in T cells, promoting tumor escape mechanisms in breast cancer[49]. Notably, we have previously identified TSP5, a member of the thrombospondin family, as significantly enriched in T2D-derived exosomes compared to those from ND[10]. In contrast, ND*exo*-PDOs exhibited specific activity in the CypA pathway, which is known to significantly limit tumor growth and enhance antitumor immunity[50]. This ligand-receptor analysis further substantiates the role of T2D-derived exosomes in fostering a more aggressive and immune-suppressed TME.

Discussion

T2D has long been established as a risk factor for poorer prognosis of breast cancer across numerous population studies[1]. Epidemiological data indicate that women with T2D have a higher incidence of breast cancer compared to ND and they often present with more aggressive tumor

phenotypes[51]. Meta-analyses and large-cohort studies have reinforced these findings, suggesting that metabolic dysregulation in T2D may contribute to the pathogenesis and progression of breast cancer[52]. Much of the existing research has focused on tumor-intrinsic properties, including insulin-like growth factor signaling and excess glucose availability feeding tumor growth[1]. However, the role of the TME in this comorbidity has been largely overlooked. In this study, we aimed to investigate the impact of metabolic dysregulation in T2D on breast cancer aggressiveness and TME dynamics.

Exosomes have emerged as critical mediators of intercellular communication, enhancing cancer progression across various tumor types[6]. Of particular interest, plasma-derived exosomes from individuals with T2D have been shown to induce upregulation of gene sets associated with EMT, invasion, metastasis, and CSC formation in cancer cell lines[10,11]. Despite their significant influence on recipient cell behavior, it remains unclear how T2D-derived exosomes may alter niche dynamics within the TME. In this study, we extended our previous findings by utilizing PDOs to investigate exosomal signaling within the breast TME. By examining these communication networks, we sought to elucidate how exosomes contribute to breast cancer aggressiveness in the context of T2D. We used plasma-derived exosomes to simulate the influence of T2D-associated systemic factors on the TME. Although this approach does not entirely capture the complexity of PDOs from T2D samples, it provided a robust platform for exploring how T2D-derived exosomes contribute to a more aggressive and immune-suppressed TME.

Here, we describe a novel breast cancer PDO methodology that facilitates *in vitro* TME study by uniquely preserving native TILs and stroma. Whereas previous researchers have generated organoids that include primary TILs[16], these methods have not been established for breast cancer. Our approach, characterized by a short-term culture, offers advantages for experimental throughput and timely data acquisition that accelerates the pace of research and potential therapeutic development. By preserving native TIL populations, our model system allows for accurate modeling of human tumor-immune interactions, as opposed to traditional epithelial-only organoid models[53,54], or models that rely on the co-

culture reconstitution of peripheral blood [55,56]. Importantly, our method maintains a diverse array of endogenous immune cell types, including B cells and macrophages, alongside T cells, unlike reconstitution models that use clonally expanded or TCR-engineered populations[57].

In this study, we found that T2D*exo*-PDOs displayed enhanced EMT and CSC characteristics compared to ND*exo*-PDOs. Specifically, we observed upregulation of multiple gene sets related to these pathways[44], including NOTCH signaling, WNT signaling, EMT, migration, and multi-cancer invasiveness signatures (Fig. 2a,c,d). Pseudotime analysis revealed distinct modules of co-regulated gene expression, with Module 5 marked by EMT genes (Fig. 4d). Ligand-receptor analysis further highlighted the influence of NOTCH signaling on intercellular communication in T2D*exo*-PDOs (Fig. 6e). Morphological assessments supported these findings, as T2D*exo*-PDOs displayed pronounced budding (Fig. 2e,f). The networks that we see perturbed are remarkably similar to what we have already published in multiple T2D exosome models including breast cancer cell lines[10,11,29], suggesting a conserved mechanism of action of exosomes. These findings underscore the profound impact of metabolic dysregulation on breast cancer progression, highlighting the need for targeted therapeutic strategies that address the altered niche dynamics induced by T2D-derived exosomes.

In contrast, we observed suppression of immune function in T2D*exo*-PDOs compared to ND*exo*-PDOs, characterized by downregulation of gene sets related to multiple steps of immune function, including cytotoxic T cell signaling, T cell activation, cytokine production, and T cell proliferation (Fig. 2a,c). Restricting our analyses to the immune compartment, we further highlighted the upregulation of IL-10 signaling and hypoxia signatures with concurrent downregulation of immune activation and immune effector function in T2D*exo*-PDOs (Fig. 5d). A deeper analysis of the immune state dynamics revealed expansion of ChopT cells (Fig. 5a, Fig. S5a-c), a distinct and conserved T cell state indicative of ER stress. Interestingly, we highlighted T2D*exo*-specific TRAIL signaling (Fig. 6e), which has been linked to unfolded protein response[47]. Notably, thrombospondin signaling was also specifically active in T2D*exo*-

T cells (Fig. 6g), aligning with our previous findings of TSP5 upregulation in T2D-derived exosomes compared to ND controls[10]. This finding highlights the significant role of thrombospondin family proteins in exosome effector function, influencing not only tumor cells but also the broader TME. Interestingly, we did not observe a significant change in Teff proportions, contrary to what might be expected in the pro-tumorigenic TME in T2D; instead, there was contraction of MAIT cells (Fig. 5c), consistent with reports of diminished MAIT frequency and functionality in adults with T2D, particularly in obese patients[58,59]. Collectively, these results suggest a pattern of immune evasion in T2D, driven by ER stress and altered cytokine signaling likely driven by the hypoxic conditions prevalent in the TME.

Contrary to our expectations, we did not observe upregulation of checkpoint ligands on T cells, which would have rendered them exhausted. Immune exhaustion is a critical issue for cancer patients, characterized by upregulation of inhibitory receptors of T cells that leads to impaired immune function[5]. Exhaustion phenotypes have been shown to worsen with T2D, contributing to poorer clinical outcomes[4]. However, the distinct immune profile seen in our study suggests an alternative pattern of dysfunction. Critically, immune checkpoint blockade therapy, which aims to reverse T cell exhaustion by targeting these inhibitory pathways, would likely be ineffective in this context. This result is consistent with existing literature reporting a diminished response to immunotherapy in T2D cancer patients[60,61]. Given the unique immune landscape in breast cancer with comorbid T2D, therapeutic strategies need to be tailored to address the specific perturbations observed. Standard immunotherapies that focus on checkpoint inhibition may not suffice; instead, approaches that alleviate T-cell specific ER stress, modulate hypoxic responses, and enhance the overall immune function within the TME might prove more effective.

Our research primarily focused on ER+ tumors, providing valuable insights into the breast cancer TME in the context of T2D. However, we recognize the importance of extending these findings to other breast cancer subtypes, particularly ER- and triple negative breast cancers, which are more prevalent in individuals with T2D[51]. We are actively expanding our studies to include these subtypes with the aim of

broadening the applicability of our findings and providing a more comprehensive understanding of the TME across diverse breast cancer populations. Additionally, while our current study did not investigate how patient metabolic medications might influence exosome payloads, future studies will explore this important aspect. Understanding the impact of factors such as diet, exercise, and weight loss medications on exosome-mediated signaling could uncover potential anti-metastatic and anti-immune evasive benefits mediated by specific miRNAs.

Together, these findings enhance our understanding of dynamic interactions within the TME and offer new insights into the significance of novel exosomal communication on tumor biology. Our results suggest that metabolic status, particularly T2D, could be considered in the clinical management of ER+ breast cancer to improve therapeutic outcomes. Given the unique vulnerabilities of this population, we strongly advocate for the initiation of targeted clinical trials to explore the TME in these 120 million underserved and understudied patients. Addressing these gaps in knowledge and care could pave the way for more effective, personalized treatment strategies, ultimately improving survival and quality of life for this high-risk group.

Methods

Patient sample collection

This study was conducted with approval from the Boston University (BU) Institutional Review Board (IRB), ensuring adherence to ethical standards. Informed consent was obtained from each participant prior to enrollment. Breast tumor tissues were harvested from three patients with histologically confirmed ER+ breast cancer during resection surgery. None of the patients had received chemotherapy or radiotherapy prior to surgery, avoiding potential confounders in tumor biology. The collected tissues were processed immediately after resection. Samples were aseptically minced into approximately $1mm^3$ chunks using sterile scalpel blades, facilitating even freezing and subsequent thawing. Chunks were then

cryopreserved in Cryostor® CS10 freezing media (StemCell, #100-1061), designed to minimize cryoinjury, at a controlled cooling rate of -1°C per minute, and stored at -196°C until further processing.

Tissue digestion and organoid generation

PDOs were cultured from cryopreserved breast tumor samples following a modified version of previously published protocols[13,53,54]. A two-step enzymatic digestion process was implemented to ensure gentle dissociation while preserving vital stromal and immune subsets. Initially, tissues were incubated at 37°C for 1 hr under 200 rpm with 2 mg/mL collagenase III (StemCell, #07422) in a complete medium consisting of Hyclone DMEM/F/12 1:1 (Thermo Scientific, #SH30023.01) supplemented with 15mM HEPES, 2.5mM L-glutamine, 10 µg/mL gentamicin (Sigma, #G1272), 1% penicillin/streptomycin (Sigma, #516106), 2.5 µg/mL Amphotericin B (Fisher, #MT30003CF), 5mM nicotinamide (Sigma, #N0636), 1.25 mM N-acetylcysteine (Sigma, #A9165), 1x B27 supplement (Fisher, 17-504-044), 250 ng/mL R-spondin 3 (Sigma, #SRP3323), 5 nM heregulin (StemCell, #78071), 5ng/mL KGF (StemCell, #78046), 20 ng/mL FGF10 (StemCell, #78037), 5ng/mL EGF (StemCell, #78006), 100 ng/mL Noggin (StemCell, #78060), 500 nM A83-01 (StemCell, #72022), 5 µM Y-27632 (Fisher, #72302), and 500 nM SB202190 (Sigma, #S7067). After this initial digestion, the supernatant containing small cell clusters was carefully removed. Fresh digestion medium was then added to the remaining larger tissue chunks for an additional hour to complete the dissociation process. Following digestion, tissue chunks were washed with DMEM/F12 and passed through a pre-wetted 100 µm filter to remove any undigested fragments and debris. The flow-through was then pelleted and resuspended in Geltrex® (Thermo, #A1413201) BME at 4°C then seeded to form domes in pre-warmed 24-well plates. Plates were inverted and allowed to polymerize at 37°C for 30 min. Subsequently, 500 µL of pre-warmed complete medium was gently added per 35 µL BME dome to maintain the PDOs. After initial seeding, PDOs were cultured for only 3 days

prior to any downstream treatments in order to maintain native TIL populations, ensuring their viability and functionality for subsequent analyses.

Exosome isolation and characterization

Patient whole blood was collected from noncancerous individuals at the Boston Medical Center Diabetes Clinic following IRB-approved protocols and with informed consent. The blood samples, one from a diabetic donor (HbA1c 9.3%) and one from a ND donor, were used exclusively for exosome isolation and were not associated with the individuals from whom breast tumor tissues were obtained for PDO generation. Blood samples were centrifuged at 16,000 rpm at 4°C for 30 min to separate plasma, which was then further clarified by additional centrifugation and filtration through a 0.2 µm filter to remove large vesicles or apoptotic bodies. Plasma was prepared to be platelet free and isolated within 30 minutes of the blood collection. Exosomes were isolated using size exclusion chromatography with qEV columns (IZON, product code 1CS-35) equipped with spherical beads featuring 35 nm pore sizes, fractionating exosomes ranging from 35 nm to 150 nm in diameter. To minimize experimental variability and focus on the most informative metabolic contrasts, we selected exosome donors through a targeted screening process. The T2D donor was chosen based on having the highest HbA1c level among those not on metabolic drugs, including metformin. The ND donor selected was not taking any medications. Preliminary screening indicated that exosomes from this T2D patient produced the most pronounced differences between the treatment group and negative control. Purified exosomes were eluted in DMEM/F12 and stored at 4°C. Storage of the isolated exosomes was short term (<24 hours post isolation). Size distribution and concentration of exosomes were measured using a NanoSight NS300 system (Malvern Panalytical). Quality control for the exosomal preparations was performed according to previously published protocols[10,11].

Exosome treatment

We estimated the number of cells within each PDO sample to normalize exosome treatments. Traditional cell counting methods were not suitable as they would disrupt the architecture of the PDOs; instead, we calculated the total cell number by assuming the PDOs were spherical and determining their volume. This volume was then divided by the average volume of a single cell to estimate the number of cells per PDO. This estimation process was repeated across multiple PDOs to determine an average cell count per PDO, which was then multiplied by the total number of PDOs to obtain the overall cell count for each sample. PDOs were retrieved from BME domes by liquefying the BME at 4°C for 15 min, followed by centrifugation at 500 rcf for 5 min. Exosomes were isolated from plasma samples of ND and T2D donors, yielding approximately 4.55×10^{11} and 6.57×10^{11} exosomes per milliliter of plasma, respectively. Exosome recovery was consistent between patient groups. For experimental consistency, exosomes were normalized to a concentration of 5,000 particles per PDO cell. PDOs were subsequently seeded to form BME domes into 35mm glass-bottom FluoroDish® plates (World Precision Instruments) as described above. After polymerization, 2mL of pre-warmed complete medium, supplemented with the same concentration of exosomes, was gently added to each BME dome to sustain PDO cultures. PDOs were cultured for an additional 3 days to allow for effective exosome uptake and interaction before proceeding to downstream applications.

Microscopy and imaging of organoids

Morphological assessments of PDOs were conducted via reflectance confocal microscopy using Live-Duo LSM 710 system (Zeiss, Thornwood NY) at the BU Microscopy Core, equipped with a Plan-Apochromat 20X/0.8 objective (Carl Zeiss Microscopy GmbH) and 543 nm solid state laser. PDOs were mounted directly onto FluoroDish® glass-bottom dishes, leveraging the natural refractive properties of the tissues to negate the need for staining. Images were captured at a resolution of 1024x1024 pixels to

ensure detailed visualization. Image acquisition was performed at 37°C in a humidified atmosphere containing 5% CO_2, optimal for live-cell imaging. Post-acquisition, images were processed using FIJI software[62,63]; briefly, brightness and contrast were adjusted before applying automatic thresholding. Morphological parameters including area, perimeter, and circularity of PDOs were calculated via particle analysis. Single cells were excluded by applying size filters greater than 300 µm2.

Single-cell library preparation and sequencing

PDOs were enzymatically digested into single cells using TrypLE Express (Thermo Fisher Scientific) to ensure a gentle yet effective separation. Cells were resuspended in 0.1% BSA in PBS and passed through a 40 µm cell strainer to achieve a uniform single-cell suspension. Cells were stained with DAPI to identify and exclude non-viable cells and isolated using a FACSAria cell sorter (BD Biosciences) in the BU Flow Cytometry Core. Sorted cells from each treatment group were loaded into individual wells of a 10X Chromium microfluidics chip for single-cell barcoding. Libraries were prepared using the Chromium Single Cell 3' Library & Gel Bead Kit v3.1 (10X Genomics) according to standard protocols. Quality and quantity of the amplified cDNA were assessed using an Angilent Bioanalyzer 2100 High Sensitivity Kit. Libraries were then multiplexed and sequenced on an Illumina NextSeq 2000 platform, aiming for a depth of approximately 30,000 reads per cell, which provides sufficient coverage to detect most expressed genes.

Single-cell data processing, clustering annotation, and integration

Transcriptomic data were mapped to the human reference genome (GRCh38.p14) and assigned to individual cells of origin according to cell-specific barcodes using the Cell Ranger pipeline version 6.0.1 (10X Genomics). Filtering, feature selection, clustering, and other secondary analyses were performed using Seurat v5.0.1[64]. Initial preprocessing included the removal of doublets using the DoubletFinder

v2.0.4 pipeline[65]. The data were further filtered to exclude cells with high mitochondrial gene expression (>20%) and aberrant unique feature counts (<100, >9000), followed by normalization and identification of highly variable features using scTransform v0.4.1[66]. Dimensionality reduction was carried out via PCA using 50 dimensions, followed by clustering using the graph-based Louvain method with a resolution of 0.5 to identify distinct cellular populations. Cell types within these clusters were then automatically annotated using the SingleR pipeline[22], referencing an established comprehensive single cell atlas of breast cancer patient samples[23]. To harmonize the data across patients and mitigate batch effects, we performed dataset integration using scVI[18,19] . This methodology was selected over alternatives based on *k*-nearest-neighbor batch effect test, integration local inverse Simpson's index, average silhouette width, and principal component regression comparison from single cell integration benchmarking (scIB) analysis [67].

Identification of neoplastic from normal breast epithelial cells

The integrity of tumor cells within clusters was confirmed by performing inferCNV analysis[68], which identified loss of heterozygosity and copy number alterations characteristic of tumor cells compared to normal immune cells present within PDOs. Epithelial cells were classified into normal or neoplastic categories using a method previously described[23]. Briefly, the mean of squared, scaled inferred changes at each genomic locus was used to calculate a genomic instability score for each cell. For each patient, the top 5% of cells with the highest genomic instability scores were used to generate an average CNV profile. Cells were then correlated with this profile to obtain malignancy scores and plotted accordingly.

Partitioning around medoids clustering was performed using the pamk function in the fpc v2.2.12 package to determine the optimal number of clusters based on silhouette scores. To call normal from tumor cells, a comprehensive grid search over a range of standard deviation multipliers was conducted and applied to both genomic instability and malignancy scores to maximize the average silhouette width. The resulting thresholds were confirmed through visual inspection of scatter plots and histograms of genomic

instability and malignancy scores with thresholds clearly demarcated. Thresholds were further validated by comparing expression profiles with cancer-associated genes and pathways including the COSMIC CGC[20] and GOBP_MAMMARY_EPITHELIAL_PROLIFATION[21].

Differential gene expression and pathway enrichment

Considering that data integration is performed only in the latent space leaving the raw expression profiles untouched, differential expression analysis needs to account for both biological variance and unwanted covariates such as batch effects. To model these technical effects, we performed differential expression analysis using the FindMarkers function in Seurat, using the statistical framework introduced by MAST[69] and setting a latent variable of patient batch. To further explore the biological processes and pathways associated with the differentially expressed genes, we performed functional enrichment analysis using the DAVID Knowledgebase v2024q2[34,35]. GSEA was also conducted using the FGSEA v1.26.0 package[70], drawing on gene sets from the Molecular Signatures Database (MSigDB)[24,25]. Enrichment scores were normalized, with permutations set to 50,000 times, using an adjusted p-value cut off of 0.05 to filter the significant enrichment results. Expression of specific gene sets of interest were determined by first calculating the average expression score per cell using the AddModuleScore in Seurat, then utilizing a linear mixed-effects regression (LMER) model via the lmerTest v3.1.3 package correcting for batch effect.

Differential cell type proportion analysis

To compare the abundance of different cell types between experimental conditions in our dataset, we utilized a binomial generalized linear model (GLM) framework via the lmerTest v3.1.3 package to model the count of cell types across conditions while controlling for covariates such as batch. Differential cell type proportion was then quantified as a log odds ratio, reporting the enrichment or depletion of cell types

across conditions, using estimated marginal means obtained from the binomial model via the emmeans v1.10.1 package.

Ligand-receptor analysis

Cell-cell communication within and between tumor and microenvironment populations was analyzed via CellChat v2.1.2[42,43] with default configurations. This analysis incorporated a curated database of ligand-receptor interactions, providing a statistical framework for inferring lineage-specific interactions. The T2D*exo*-PDO and ND*exo*-PDO data were extracted and formatted into CellChat format. Data processing and visualization were performed with default settings.

Pseudotemporal ordering to infer cell trajectories

Diffusion-pseudotime (DPT) analysis was performed using the Monocle3 v1.3.5 package[32]. Seurat single cell objects containing epithelial cells were converted into a Monocle object using SeuratWrappers v0.3.4 package, followed by standard clustering and trajectory inference. The trajectory was rooted in normal LECs to establish the pseudotime ordering. Differential gene expression along the trajectory was assessed using the graph_test function in Monocle3, identifying genes significantly associated with the progression of cell states. Genes were grouped into modules of co-expression via the find_gene_modules function in Monocle3. Module scores were then calculated for each cell using the AddModuleScore function in Seurat.

Statistical analysis

Statistical analyses were performed using R version 4.3.1. Specific tests are indicated in the figure legends along with the statistical significance.

Data and code availability

All raw data will be available to download from GEO. Processed data will be available for exploration on CELLxGENE. These will be publicly available at time of publication. Metadata for the different PDOs is available in Supplementary Table S1. All original code will be deposited at https://github.com/montilab/BrCaExoPDO/.

Acknowledgments

We are grateful to David Sherr, Robert Fisher, and Jason Weis for their valuable discussions on data interpretation and manuscript revision, Lina Kroehling for her advice on analysis and statistics, Vinay Duggineni and Christina McConney for their help with cell cluster annotation, and Emma Kelley and Ruben Dries for their support during the setup of the PDO platform. We appreciate the technical assistance and expertise of the BU Flow Cytometry Core Facility, Christopher Williams at the BU Single Cell Sequencing Core, Yuriy Alekseyev at the BU Microarray Sequencing Core, and Michael Kirber at the BU Cellular Imaging Core. We also thank the study nurses and clinical staff that obtained samples and the patients who generously consented for the research use of these samples. Finally, we appreciate members of the Denis and Monti laboratories as well as students and faculty in the BU Virology, Immunology, and Microbiology Department and Immunology Training Program for their feedback and support.

Author contributions

Conception and design: C.S.E., G.V.D. Methodology: C.S.E., S.M., G.V.D. Acquisition of data: C.S.E. M.S., H.K., A.I., K.M., N.K. Analysis and interpretation of data: C.S.E., A.C., S.M. Writing, editing, and revision of manuscript: C.S.E., M.S., A.C., G.V.D. Study supervision and funding: G.V.D.

Declaration of interests

The authors declare no competing interests.

References

1. Ennis, C. S., Llevenes, P., Qiu, Y., Dries, R. & Denis, G. V. The crosstalk within the breast tumor microenvironment in type II diabetes: Implications for cancer disparities. *Front Endocrinol* (2022) doi:10.3389/fendo.2022.1044670.

2. Daryabor, G., Atashzar, M. R., Kabelitz, D., Meri, S. & Kalantar, K. The Effects of Type 2 Diabetes Mellitus on Organ Metabolism and the Immune System. *Front Immunol* **11**, 1582 (2020).

3. Berbudi, A., Rahmadika, N., Tjahjadi, A. I. & Ruslami, R. Type 2 Diabetes and its Impact on the Immune System. *Curr Diabetes Rev* **16**, 442–449 (2020).

4. Nojima, I. *et al.* Dysfunction of CD8 + PD-1 + T cells in type 2 diabetes caused by the impairment of metabolism-immune axis. *Sci Rep-uk* **10**, 14928 (2020).

5. Zhang, Z. et al. T *Cell* Dysfunction and Exhaustion in Cancer. *Frontiers Cell Dev Biology* **8**, 17 (2020).

6. Yu, D. et al. Exosomes in development, metastasis and drug resistance of breast cancer. *Cancer Sci* **106**, 959–964 (2015).

7. Jafari, N., Llevenes, P. & Denis, G. V. Exosomes as novel biomarkers in metabolic disease and obesity-related cancers. *Nat. Rev. Endocrinol.* **18**, 327–328 (2022).

8. Clement, E. et al. Adipocyte extracellular vesicles carry enzymes and fatty acids that stimulate mitochondrial metabolism and remodeling in tumor cells. *EMBO J.* **39**, e102525 (2020).

9. Lehuédé, C. et al. Adipocytes promote breast cancer resistance to chemotherapy, a process amplified by obesity: role of the major vault protein (MVP). *Breast Cancer Res.* **21**, 7 (2019).

10. Jafari, N. et al. Adipocyte-derived exosomes may promote breast cancer progression in type 2 diabetes. *Sci Signal* **14**, eabj2807 (2021).

11. Jafari, N. et al. Novel plasma exosome biomarkers for prostate cancer progression in co-morbid metabolic disease. *Adv. Cancer Biol. - Metastasis* **6**, 100073 (2022).

12. LeSavage, B. L., Suhar, R. A., Broguiere, N., Lutolf, M. P. & Heilshorn, S. C. Next-generation cancer organoids. *Nat Mater* 1–17 (2021) doi:10.1038/s41563-021-01057-5.

13. Bhatia, S. et al. Patient-Derived Triple-Negative Breast Cancer Organoids Provide Robust Model Systems That Recapitulate Tumor Intrinsic Characteristics. Cancer Res **82**, 1**174**–1192 (2022).

14. Saeki, S. et al. Transcriptomic intratumor heterogeneity of breast cancer patient-derived organoids may reflect the unique biological features of the tumor of origin. Breast Cancer Res **25**, 21 (2023).

15. Tsai, K. K. et al. Screening of organoids derived from patients with breast cancer implicates the repressor NCOR2 in cytotoxic stress response and antitumor immunity. *Nat. Cancer* **3**, 734–752 (2022).

16. Neal, J. T. et al. Organoid Modeling of the Tumor Immune Microenvironment. Cell **175**, 1972-1988.e16 (2018).

17. Yuki, K., Cheng, N., Nakano, M. & Kuo, C. J. Organoid Models of Tumor Immunology. *Trends Immunol* **41**, 652–664 (2020).

18. Gayoso, A. et al. A Python library for probabilistic analysis of single-cell omics data. *Nat. Biotechnol.* **40**, 163–166 (2022).

19. Lopez, R., Regier, J., Cole, M. B., Jordan, M. I. & Yosef, N. Deep generative modeling for single-cell transcriptomics. *Nat. Methods* **15**, 1053–1058 (2018).

20. Sondka, Z. et al. The COSMIC Cancer Gene Census: describing genetic dysfunction across all human cancers. *Nat. Rev. Cancer* **18**, 6**9**6–705 (2018).

21. Carbon, S. et al. AmiGO: online access to ontology and annotation data. *Bioinformatics* **25**, 288–289 (2008).

22. Aran, D. et al. Reference-based analysis of lung single-cell sequencing reveals a transitional profibrotic macrophage. *Nat. Immunol.* **20**, 163–**172** (20**19**).

23. Wu, S. Z. et al. A single-cell and spatially resolved atlas of human breast cancers. *Nat Genet* **53**, 1334–1347 (2021).

24. Mootha, V. K. et al. PGC-1α-responsive genes involved in oxidative phosphorylation are coordinately downregulated in human diabetes. *Nat. Genet.* **34**, 267–273 (2003).

25. Subramanian, A. et al. Gene set enrichment analysis: A knowledge-based approach for interpreting genome-wide expression profiles. *Proc. Natl. Acad. Sci.* **102**, 15545–15550 (2005).

26. Brabletz, T., Kalluri, R., Nieto, M. A. & Weinberg, R. A. EMT in cancer. Nat. Rev. Cancer 18, 128–134 (2018).

27. Karolak, A., Poonja, S. & Rejniak, K. A. Morphophenotypic classification of tumor organoids as an indicator of drug exposure and penetration potential. *PLoS Comput. Biol.* **15**, e1007214 (2019).

28. Mukashyaka, P. et al. High-throughput deconvolution of 3D organoid dynamics at cellular resolution for cancer pharmacology with Cellos. *Nat. Commun.* **14**, 8406 (2023).

29. Qiu, Y. et al. Insulin Resistance Increases TNBC Aggressiveness and Brain Metastasis via Adipocyte-derived Exosomes. *bioRxiv* 2024.05.01.592097 (2024) doi:**10**.1101/2024.05.01.592097.

30. Zhang, X., Powell, K. & Li, L. Breast Cancer Stem Cells: Biomarkers, Identification and Isolation Methods, Regulating Mechanisms, Cellular Origin, and Beyond. *Cancers* **12**, 3765 (2020).

31. Gabriely, G. et al. MicroRNA 21 Promotes Glioma Invasion by Targeting Matrix Metalloproteinase Regulators. *Mol. Cell. Biol.* **28**, 5369–5380 (2008).

32. Cao, J. et al. The single-cell transcriptional landscape of mammalian organogenesis. *Nature* **566**, 496–502 (2019).

33. Cornel, A. M., Mimpen, I. L. & Nierkens, S. MHC Class I Downregulation in Cancer: Underlying Mechanisms and Potential Targets for Cancer Immunotherapy. Cancers 12, 1760 (2020).

34. Sherman, B. T. et al. DAVID: a web server for functional enrichment analysis and functional annotation of gene lists (2021 update). *Nucleic Acids Res.* **50**, W216–W221 (2022).

35. Huang, D. W., Sherman, B. T. & Lempicki, R. A. Systematic and integrative analysis of large gene lists using DAVID bioinformatics resources. *Nat. Protoc.* **4**, 44–57 (2009).

36. Gahete, M. D. et al. Changes in Splicing Machinery Components Influence, Precede, and Early Predict the Development of Type 2 Diabetes: From the CORDIOPREV Study. *EBioMedicine* **37**, 356–365 (2018).

37. O'Neill, C., Cassidy, F. C., O'Shea, D. & Hogan, A. E. Mucosal Associated Invariant T Cells in Cancer-Friend or Foe? Cancers **13**, 1582 (2021).

38. Cao, Y. et al. ER stress-induced mediator C/EBP homologous protein thwarts effector T cell activity in tumors through T-bet repression. Nat. Commun. 10, 1280 (2019).

39. Thaxton, J. E. et al. Modulation of Endoplasmic Reticulum Stress Controls CD4+ T-cell Activation and Antitumor Function. *Cancer Immunol. Res.* **5**, 666–675 (2017).

40. Mirlekar, B. Tumor promoting roles of IL-10, TGF-β, IL-4, and IL-35: Its implications in cancer immunotherapy. *SAGE Open Med.* **10**, 20503121211069012 (2022).

41. Croft, M. The role of TNF superfamily members in T-cell function and diseases. *Nat. Rev. Immunol.* **9**, 271–285 (2009).

42. Jin, S., Plikus, M. V. & Nie, Q. CellChat for systematic analysis of cell-cell communication from single-cell and spatially resolved transcriptomics. bioRxiv 2023.11.05.565674 (2023) doi:10.1101/2023.11.05.565674.

43. Jin, S. et al. Inference and analysis of cell-cell communication using CellChat. Nat. Commun. 12, 1088 (2021).

44. Edwards, A. & Brennan, K. Notch Signalling in Breast Development and Cancer. *Front. Cell Dev. Biol.* **9**, 692173 (2021).

45. Ehata, S. & Miyazono, K. Bone Morphogenetic Protein Signaling in Cancer; Some Topics in the Recent **10** Years. Front. Cell Dev. Biol. 10, 883523 (2022).

46. Westermarck, J. & Kähäri, V. Regulation of matrix metalloproteinase expression in tumor invasion. *FASEB J.* **13**, 781–792 (1999).

47. Sag, D., Ayyildiz, Z. O., Gunalp, S. & Wingender, G. The Role of TRAIL/DRs in the Modulation of Immune Cells and Responses. Cancers 11, 1469 (2019).

48. Zhou, C., Gao, Y., Ding, P., Wu, T. & Ji, G. The role of CXCL family members in different diseases. *Cell Death Discov.* **9**, 212 (2023).

49. Marcheteau, E. et al. Thrombospondin-1 Silencing Improves Lymphocyte Infiltration in Tumors and Response to Anti-PD-1 in Triple-Negative Breast Cancer. Cancers 13, 4059 (2021).

50. Kalinina, A. et al. Cyclophilin A is a factor of antitumor defense in the early stages of tumor development. *Int. Immunopharmacol.* **94**, 107470 (2021).

51. Palmer, J. R., Castro-Webb, N., Bertrand, K., Bethea, T. N. & Denis, G. V. Type II Diabetes and Incidence of Estrogen Receptor Negative Breast Cancer in African American Women. Cancer Res **77**, 6462–6469 (2017).

52. Charlot, M. et al. Diabetes and breast cancer mortality in Black women. *Cancer Cause Control* **28**, 61–67 (2017).

53. Mazzucchelli, S. et al. Establishment and Morphological Characterization of Patient-Derived Organoids from Breast Cancer. *Biol Proced Online* **21**, 12 (2019).

54. Sachs, N. et al. A Living Biobank of Breast Cancer Organoids Captures Disease Heterogeneity. Cell 172, 373-386.e10 (2018).

55. Dijkstra, K. K. et al. Generation of Tumor-Reactive T Cells by Co-culture of Peripheral Blood Lymphocytes and Tumor Organoids. Cell 174, 1586-1598.e12 (2018).

56. Cattaneo, C. M. et al. Tumor organoid–T-cell coculture systems. *Nat Protoc* **15**, 15–39 (2020).

57. Meng, Q. et al. Empirical identification and validation of tumor-targeting T cell receptors from circulation using autologous pancreatic tumor organoids. *J. Immunother. Cancer* **9**, e003213 (2021).

58. Carolan, E. et al. Altered Distribution and Increased IL-17 Production by Mucosal-Associated Invariant T Cells in Adult and Childhood Obesity. *J. Immunol.* **194**, 5775–5780 (2015).

59. Magalhaes, I., Kiaf, B. & Lehuen, A. iNKT and MAIT Cell Alterations in Diabetes. *Front. Immunol.* **6**, 341 (2015).

60. Andrieu, G. P. et al. BET proteins in abnormal metabolism, inflammation, and the breast cancer microenvironment. *J Leukocyte Biol* **104**, 265–274 (2018).

61. Cortellini, A. et al. Type 2 Diabetes Mellitus and Efficacy Outcomes from Immune Checkpoint Blockade in Patients with Cancer. *Clin. Cancer Res.* **29**, 2714–2724 (2023).

62. Schindelin, J. et al. Fiji: an open-source platform for biological-image analysis. Nat. Methods 9, 676–682 (2012).

63. Schneider, C. A., Rasband, W. S. & Eliceiri, K. W. NIH Image to ImageJ: 25 years of image analysis. Nat. Methods 9, 671–675 (2012).

64. Hao, Y. et al. Dictionary learning for integrative, multimodal and scalable single-cell analysis. Nat. Biotechnol. 42, 293–304 (2024).

65. McGinnis, C. S., Murrow, L. M. & Gartner, Z. J. DoubletFinder: Doublet Detection in Single-Cell RNA Sequencing Data Using Artificial Nearest Neighbors. *Cell Syst.* **8**, 329-337.e4 (2019).

66. Choudhary, S. & Satija, R. Comparison and evaluation of statistical error models for scRNA-seq. *Genome Biol.* **23**, 27 (2022).

67. Luecken, M. D. et al. Benchmarking atlas-level data integration in single-cell genomics. Nat. Methods 19, 41–50 (2022).

68. Patel, A. P. et al. Single-cell RNA-seq highlights intratumoral heterogeneity in primary glioblastoma. *Science* **344**, 1396–1401 (2014).

69. Finak, G. et al. MAST: a flexible statistical framework for assessing transcriptional changes and characterizing heterogeneity in single-cell RNA sequencing data. Genome Biol. **16**, 278 (2015).

70. Korotkevich, G. et al. Fast gene set enrichment analysis. bioRxiv 060012 (2021) doi:10.1101/060012.

Figures

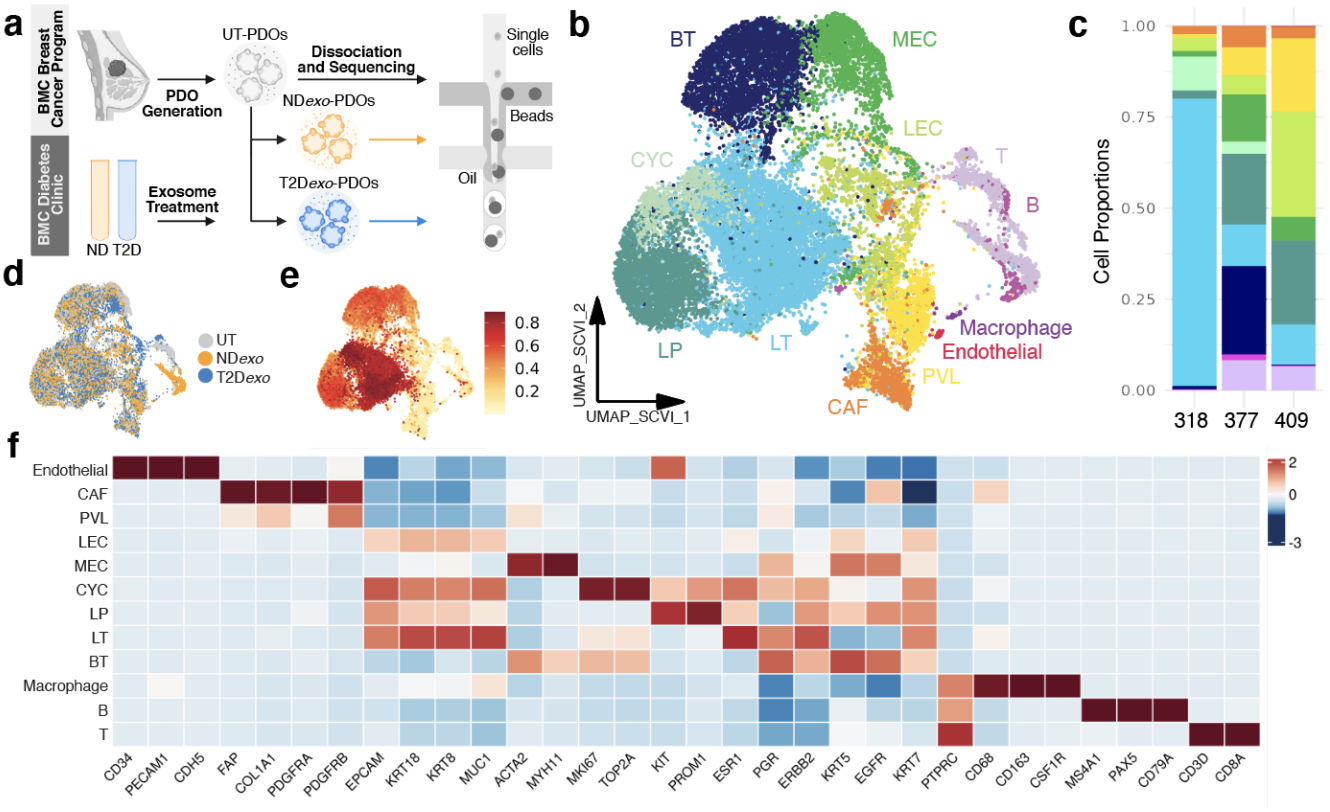

Fig 1: Cellular characterization of PDOs.

a. Illustration of scRNAseq workflow in PDO model of breast cancer TME. **b.** scVI-integrated UMAP visualization of PDOs colored by broad cell type annotation. N = 24,599 from three patients. BT (4,226 cells) denotes basal-like tumor cells; CAF (1,149 cells) denotes cancer-associated fibroblasts; CYC (1,223 cells) denotes cycling epithelial cells; LEC (1,254 cells) denotes normal luminal epithelial cells; LT (7,514 cells) denotes luminal-like tumor cells; MEC (2,382 cells) denotes normal myoepithelial cells; PVL (1,487 cells) denotes perivascular-like cells. **c.** Relative proportion of cell types in each patient highlighting conservation of major lineages. Colors denote the same cell types in A. **d/e.** scVI-integrated UMAP colored by treatment (**d**) and malignancy score as calculated from genomic instability (**e**). **f.** Heatmap showing expression of canonical marker genes per lineage.

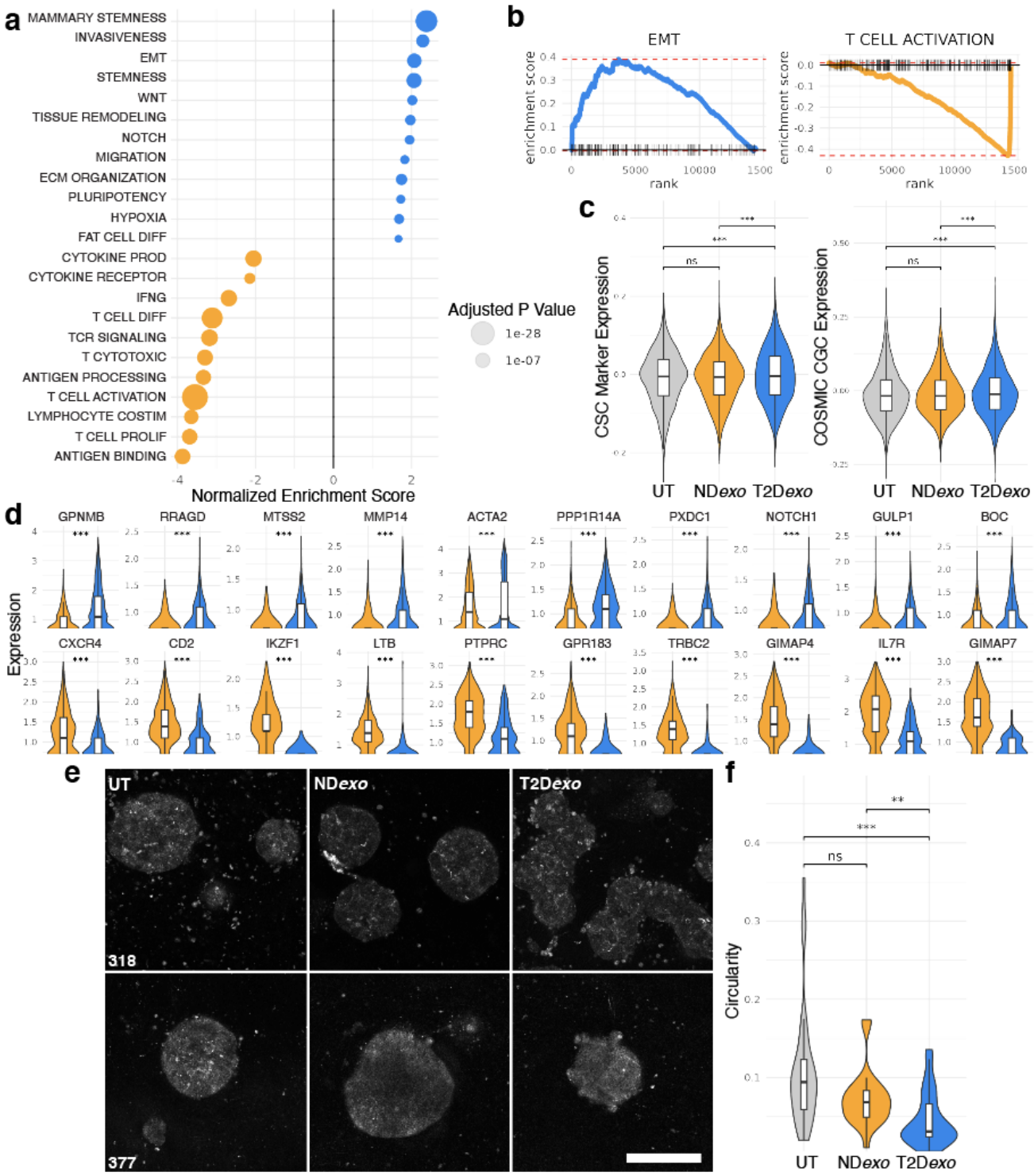

Fig 2: Increased aggression in T2D*exo*-PDOs compared to ND*exo*-PDOs.

a. Bubble plot summarizing statistically significant gene sets enriched in differentially expressed gene sets between T2D*exo*-PDOs (blue) and ND*exo*-PDOs (orange) identified with gene set enrichment analysis

(GSEA). Size of dot is scaled to adjusted p value. **b.** GSEA enrichment plots for representative gene sets upregulated (top) and downregulated (bottom) in T2D*exo*-PDOs compared to ND*exo*-PDOs. **c.** Violin plots of COSMIC CGC (left) and canonical CSC gene expression (right). Significance calculated via linear mixed effects model, ***<0.001, **<0.01, *<0.05. **d**. Violin plots of top differentially expressed genes. **e.** Representative confocal images of UT (left), ND*exo* (middle) and T2D*exo* (right) per patient. Scale bar = 100 µm. **f.** Violin plots of calculated circularity of PDOs. Singlets were removed during thresholding. Significance calculated via pairwise Wilcoxon Rank Sums test with Bonferroni correction, ***<0.001, **<0.01, *<0.05.

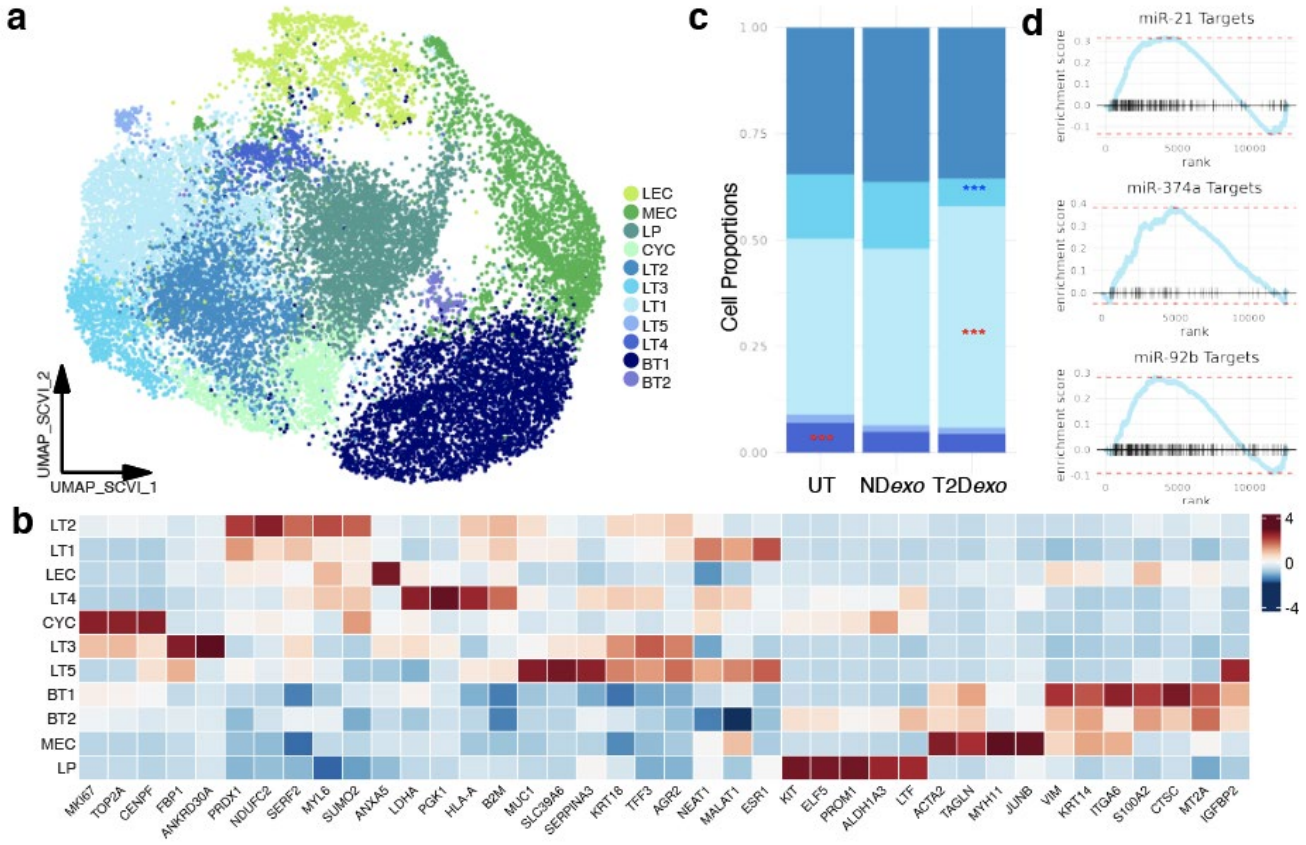

Fig 3: Tumor population dynamics in T2D*exo*-PDOs.

a. UMAP visualization of reclustered scVI-integrated epithelial cells. BT1-2 (n = 4,084; n = 142) denote basal-like tumor subclones; CYC (n = 1,223) denotes cycling epithelial cells; LEC (n = 1,254) denotes normal luminal epithelial cells; LP (n = 3,574) denotes luminal progenitor cells; LT1-5 (n = 3,397; n = 2,669; n = 925; n = 398; n = 125) denote luminal-like tumor subclones; MEC (n = 2,382) denotes normal myoepithelial cells. **b.** Heatmap showing expression of canonical and top differentially expressed marker genes per subclone. **c.** Relative proportion of luminal-like tumor subclones per treatment group. Red (blue) stars indicate significantly expanding (contracting) clusters. Significance calculated via binomial linear regression model, ***<0.001, **<0.01, *<0.05. **d.** GSEA enrichment plots for representative gene sets upregulated in LT1. miR targets determined from miRDB.

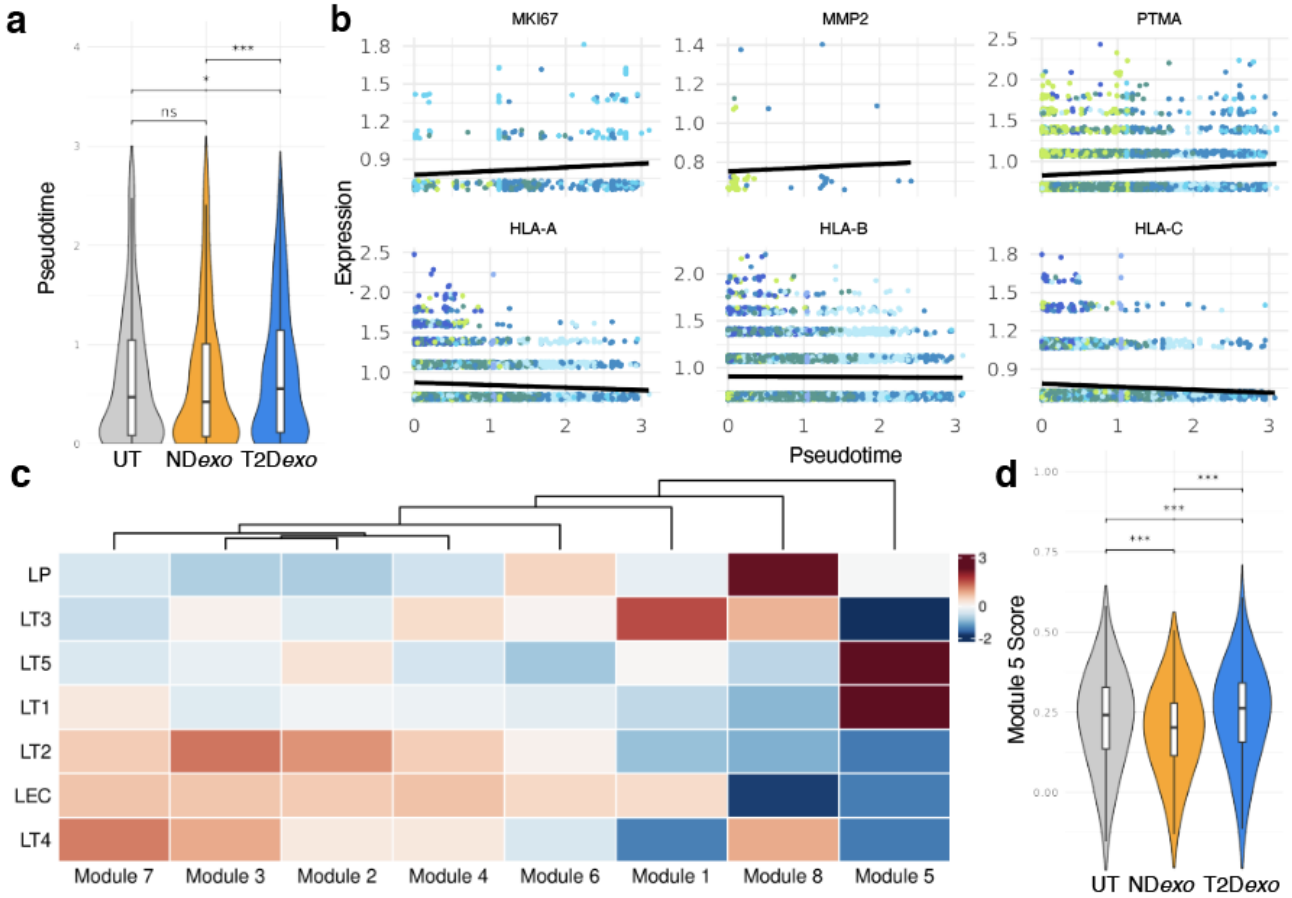

Fig 4. Tumor cell evolution.

a. Violin plots of pseudotime calculated for luminal-like epithelial cells per treatment group. Significance calculated via linear mixed effects model, ***<0.001, **<0.01, *<0.05. **b.** Scatter plots of gene expression as a function of pseudotime. Dot color denotes epithelial cell subtype assigned to cells. Black line showing linear regression of best fit. Genes determined via graph autocorrelation. **c.** Heatmap of gene module expression in epithelial cell subtypes. **d.** Violin plots of expression of Module 5 in luminal-like epithelial cells. Significance calculated via linear mixed effects model, ***<0.001, **<0.01, *<0.05.

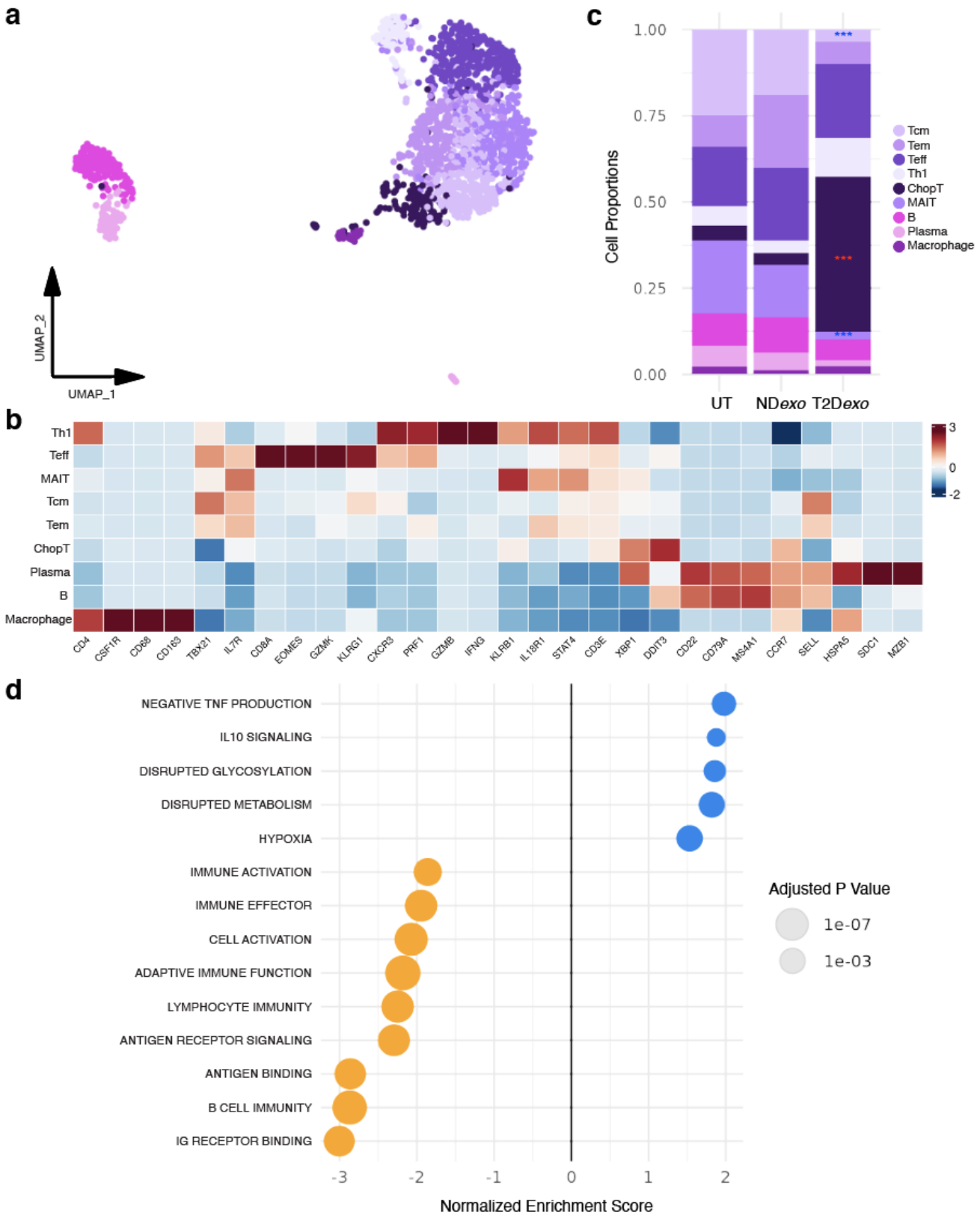

Fig 5: Perturbed immune signaling in T2D*exo*-PDOs.

a. Unintegrated UMAP visualization of clustered immune cells. ChopT (n = 135) denote *DDIT3*+ T cells; MAIT (n = 284) denote mucosal-associated invariant T cells; Tcm (n = 343) denotes central memory T cells; Tem (n = 274) denotes effector memory T cells; Teff (n = 374) denotes effector T cells; Th1 (n = 90) denote T helper 1 cells. **b**. Relative proportion of immune compartment per treatment. Red (blue) stars indicate significantly expanding (contracting) clusters. Significance calculated via binomial linear regression model, ***<0.001, **<0.01, *<0.05. **c.** Heatmap showing expression of canonical marker genes per immune cell state. **d.** Bubble plot summarizing statistically significant gene sets enriched in differentially expressed genes between the immune compartments of T2D*exo*-PDOs (blue) and ND*exo*-PDOs (orange) identified during gene set enrichment analysis (GSEA). Size of dot is scaled to adjusted p value.

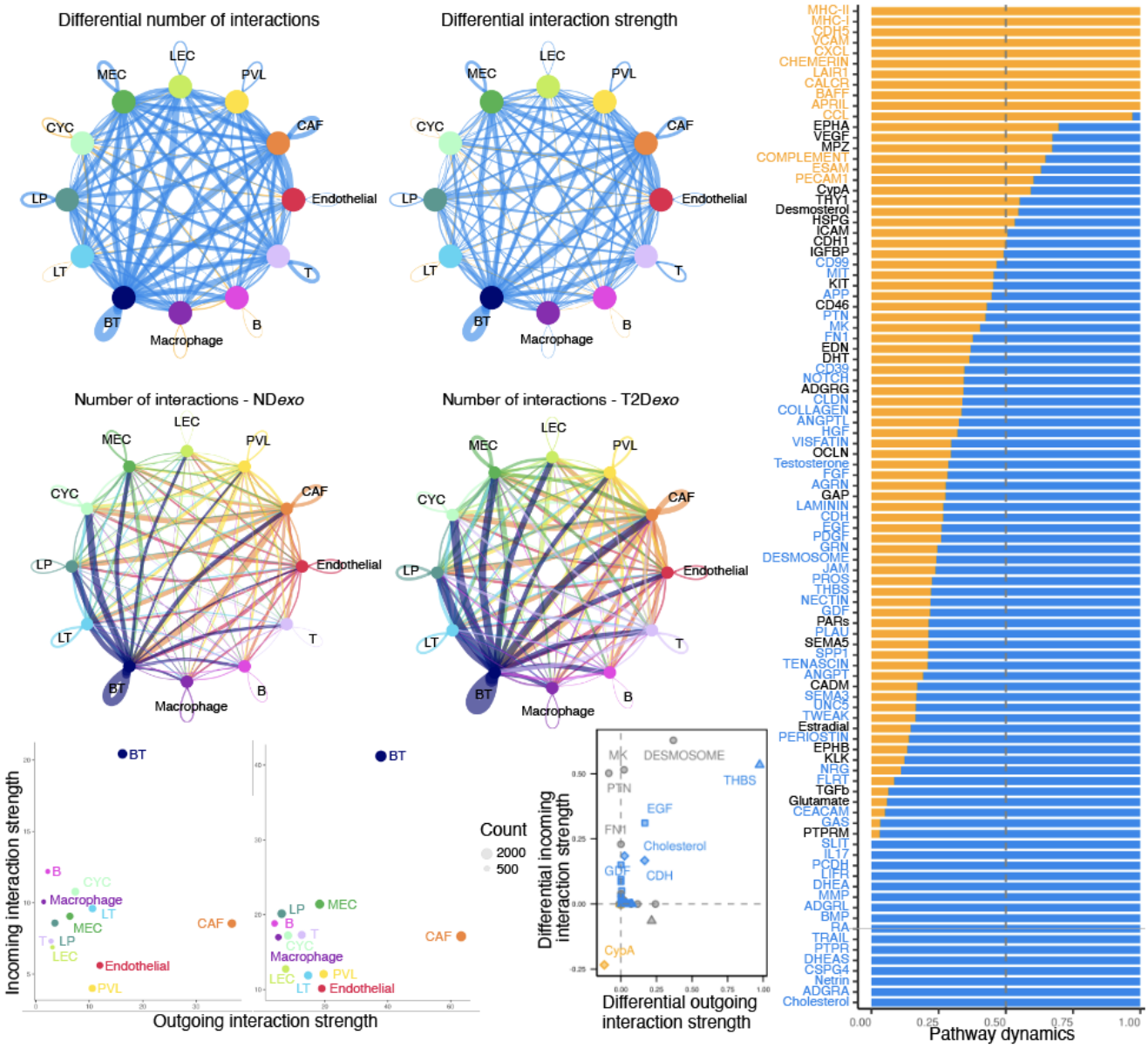

Fig 6. T2D*exo* modulates intercellular communication networks.

a. Circle plot showing the number of interactions among different cell types. The blue (orange) colored edges represent increased (decreased) signaling in T2D*exo* compared to ND*exo*-PDOs. **b**. Circle plot showing the differential interaction strength among different cell types. The blue (orange) colored edges represent increased (decreased) interaction strength in T2D*exo* compared to ND*exo*-PDOs. **c/d.** Circle plot displaying the number of interactions and the strength of interactions between cell types in ND*exo*-PDOs (**c**) and T2D*exo*-PDOs (**d**). The number of lines represents the number of interactions, and the thickness

of lines is proportional to the strength of the interactions. **e.** Stacked bar plot showing the overall information flow of each significant signaling pathway ($p < 0.01$). The vertical dashed line indicates the position where the sample accounts for 50% of the overall information flow. Label color is determined by a significantly larger contribution from T2D*exo* (blue) or ND*exo*-PDOs (orange). Pathways equally important in both datasets are labeled in black. *P* value determined by paired Wilcoxon test according to CellChat. **f.** Scatter plot of dominant senders and receivers for ND*exo* (left) and T2D*exo*-PDOs (right). **g.** Scatter plot of the signaling changes associated with T cells in T2D*exo* (blue) or ND*exo*-PDOs (orange). Shared pathways are labeled in gray. Collagen and laminin pathways have been removed from plot for ease of visualization.

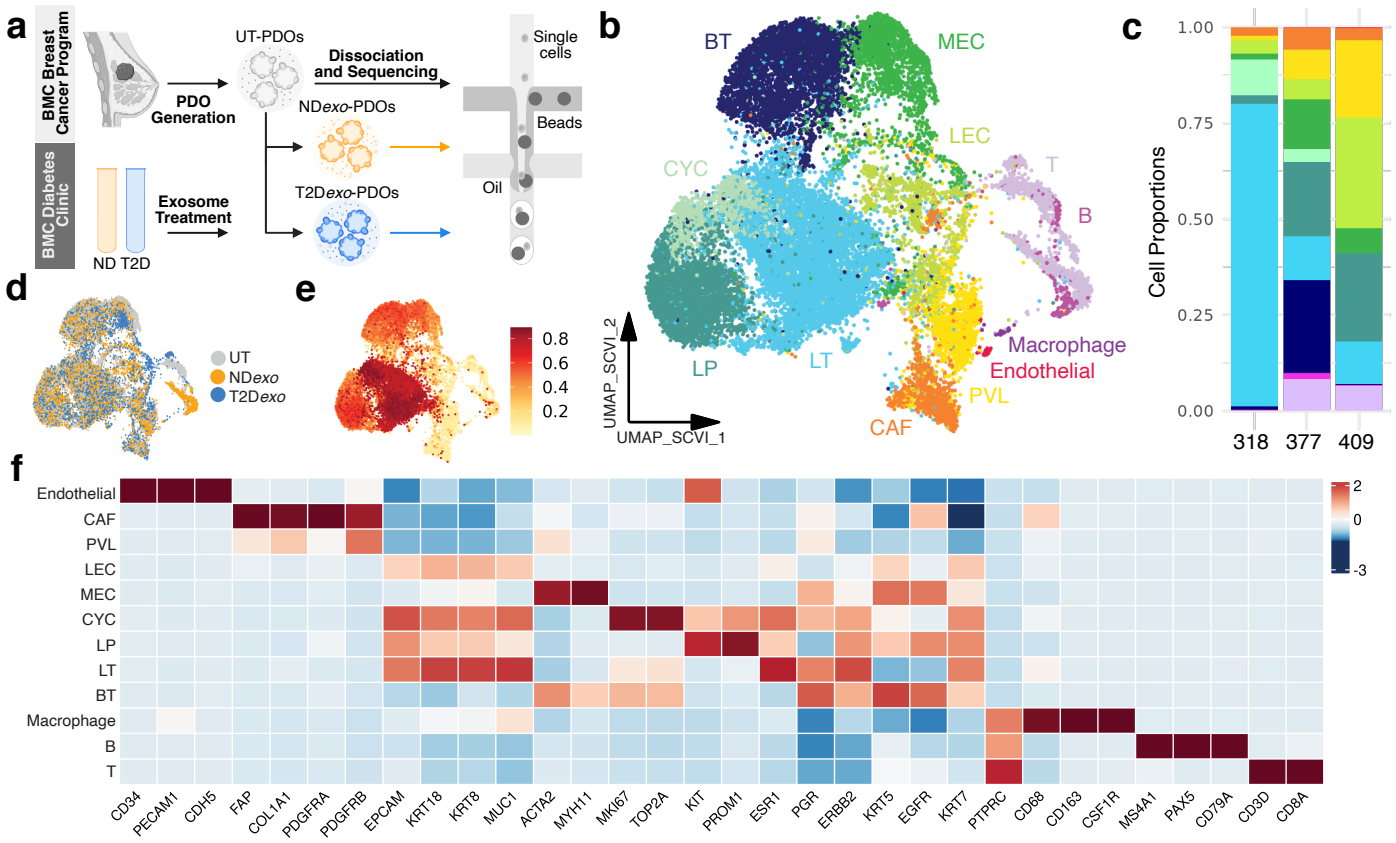
a
BMC Breast Cancer Program
BMC Diabetes Clinic
PDO Generation
UT-PDOs
Dissociation and Sequencing
Single cells
NDexo-PDOs
Beads
Exosome Treatment
T2Dexo-PDOs
Oil
ND T2D
b
BT
MEC
LEC
CYC
T
B
LP
LT
Macrophage
Endothelial
PVL
CAF
UMAP_SCVI_2
UMAP_SCVI_1
c
Cell Proportions
1.00
0.75
0.50
0.25
0.00
318
377
409
d
UT
NDexo
T2Dexo
e
0.8
0.6
0.4
0.2
f
Endothelial
CAF
PVL
LEC
MEC
CYC
LP
LT
BT
Macrophage
B
T
CD34
PECAM1
CDH5
FAP
COL1A1
PDGFRA
PDGFRB
EPCAM
KRT18
KRT8
MUC1
ACTA2
MYH11
MKI67
TOP2A
KIT
PROM1
ESR1
PGR
ERBB2
KRT5
EGFR
KRT7
PTPRC
CD68
CD163
CSF1R
MS4A1
PAX5
CD79A
CD3D
CD8A
2
0
-3

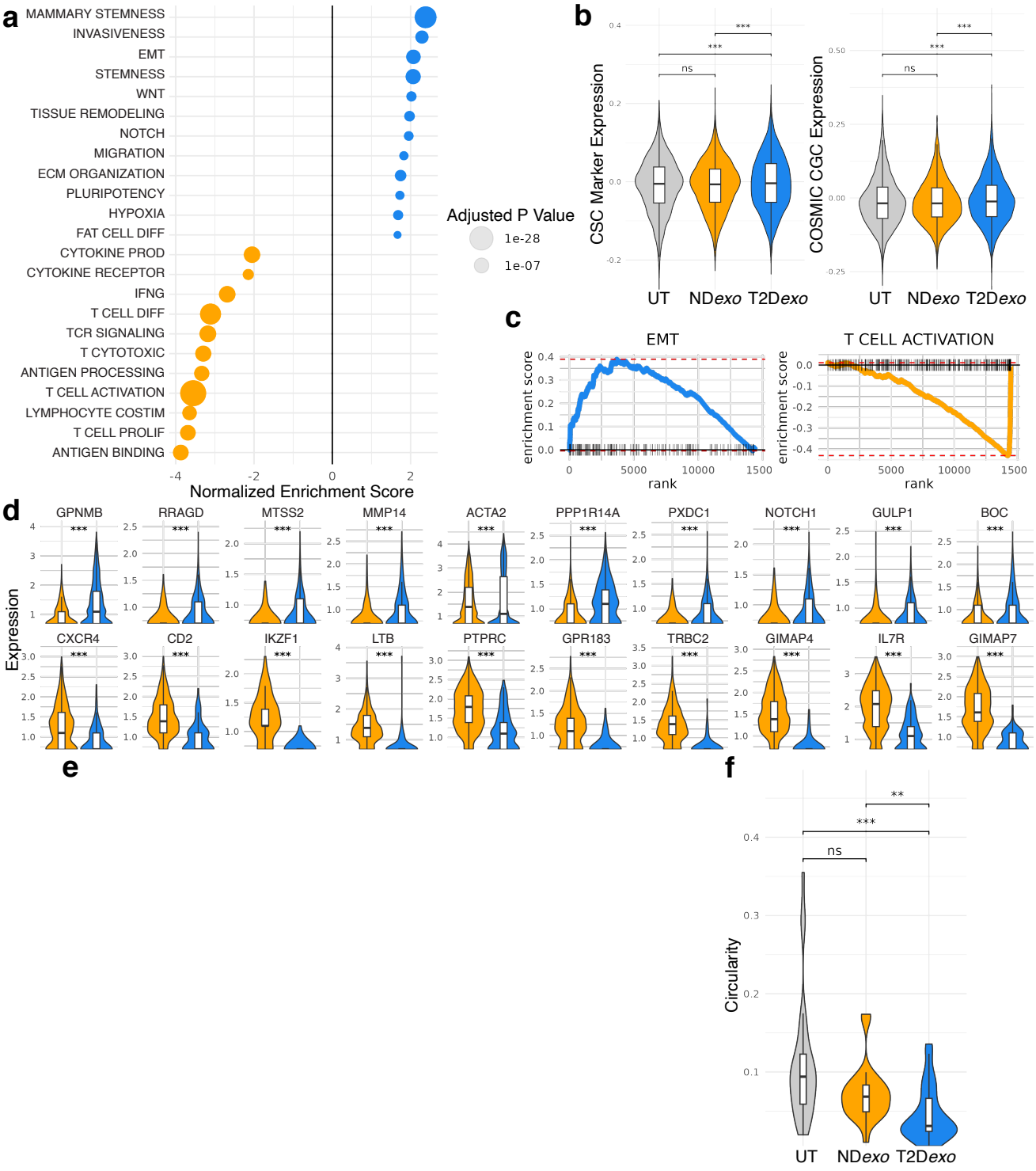
a
MAMMARY STEMNESS
INVASIVENESS
EMT
STEMNESS
WNT
TISSUE REMODELING
NOTCH
MIGRATION
ECM ORGANIZATION
PLURIPOTENCY
HYPOXIA
FAT CELL DIFF
CYTOKINE PROD
CYTOKINE RECEPTOR
IFNG
T CELL DIFF
TCR SIGNALING
T CYTOTOXIC
ANTIGEN PROCESSING
T CELL ACTIVATION
LYMPHOCYTE COSTIM
T CELL PROLIF
ANTIGEN BINDING
Normalized Enrichment Score
Adjusted P Value
1e-28
1e-07
b
CSC Marker Expression
COSMIC CGC Expression
UT
NDexo
T2Dexo
ns
***
c
EMT
T CELL ACTIVATION
enrichment score
rank
d
GPNMB
RRAGD
MTSS2
MMP14
ACTA2
PPP1R14A
PXDC1
NOTCH1
GULP1
BOC
CXCR4
CD2
IKZF1
LTB
PTPRC
GPR183
TRBC2
GIMAP4
IL7R
GIMAP7
Expression
e
f
Circularity
UT
NDexo
T2Dexo
ns
***
**

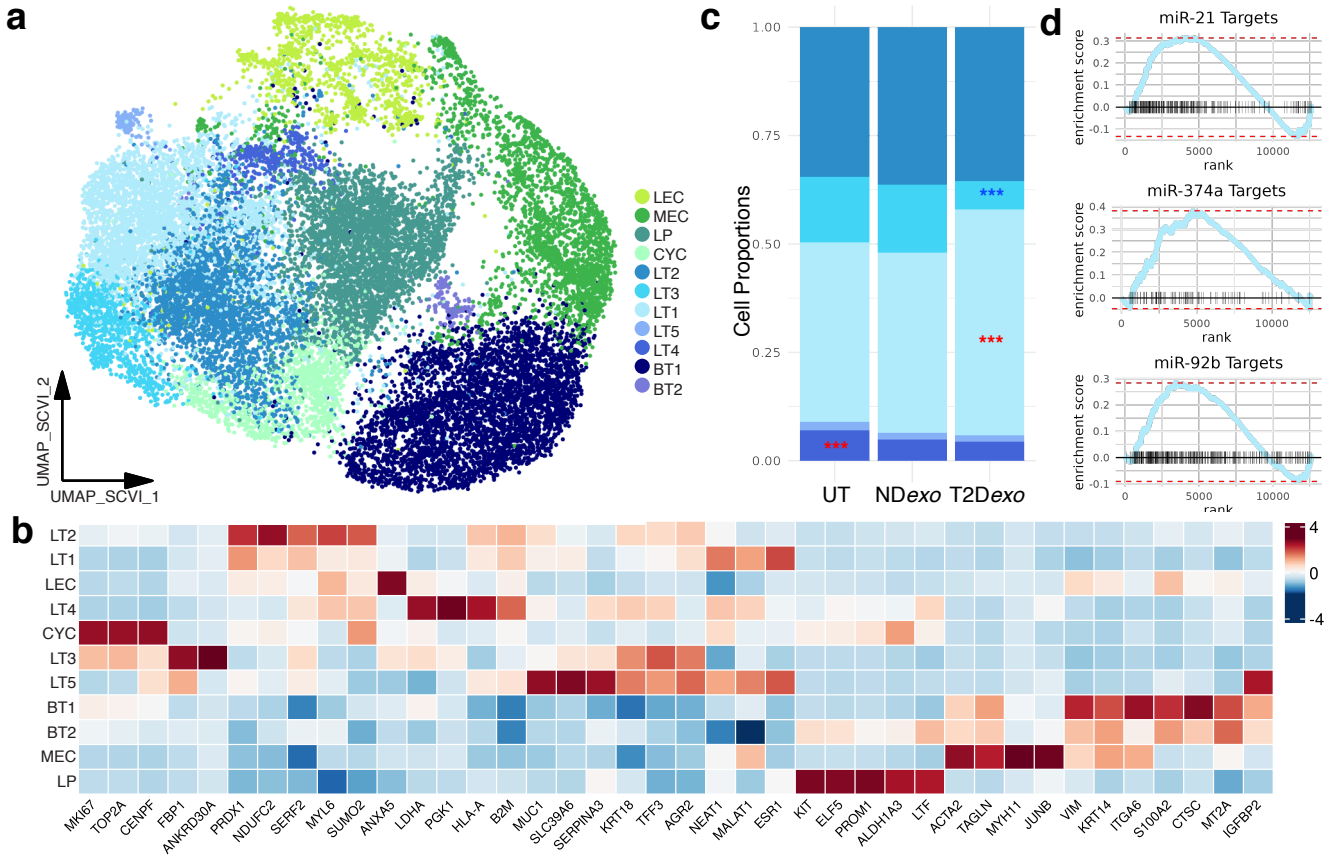
a
LEC
MEC
LP
CYC
LT2
LT3
LT1
LT5
LT4
BT1
BT2
UMAP_SCVI_2
UMAP_SCVI_1
c
Cell Proportions
1.00
0.75
0.50
0.25
0.00
***
***
***
UT
ND*exo*
T2D*exo*
d
miR-21 Targets
miR-374a Targets
miR-92b Targets
enrichment score
rank
0
5000
10000
b
LT2
LT1
LEC
LT4
CYC
LT3
LT5
BT1
BT2
MEC
LP
MKI67
TOP2A
CENPF
FBP1
ANKRD30A
PRDX1
NDUFC2
SERF2
MYL6
SUMO2
ANXA5
LDHA
PGK1
HLA-A
B2M
MUC1
SLC39A6
SERPINA3
KRT18
TFF3
AGR2
NEAT1
MALAT1
ESR1
KIT
ELF5
PROM1
ALDH1A3
LTF
ACTA2
TAGLN
MYH11
JUNB
VIM
KRT14
ITGA6
S100A2
CTSC
MT2A
IGFBP2
4
0
-4

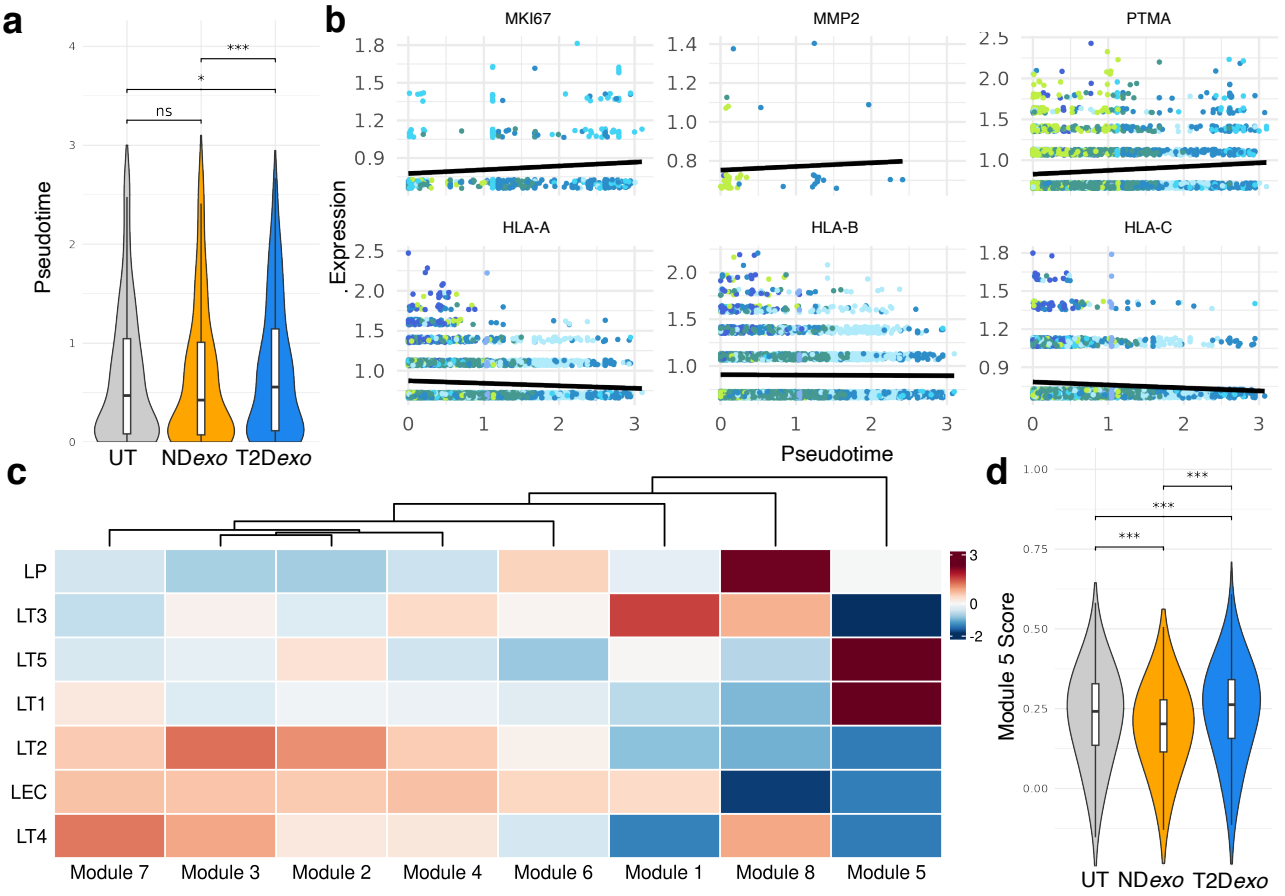
a
Pseudotime
ns
*
***
UT
NDexo
T2Dexo
b
MKI67
MMP2
PTMA
HLA-A
HLA-B
HLA-C
Expression
Pseudotime
c
LP
LT3
LT5
LT1
LT2
LEC
LT4
Module 7
Module 3
Module 2
Module 4
Module 6
Module 1
Module 8
Module 5
d
Module 5 Score
UT
NDexo
T2Dexo

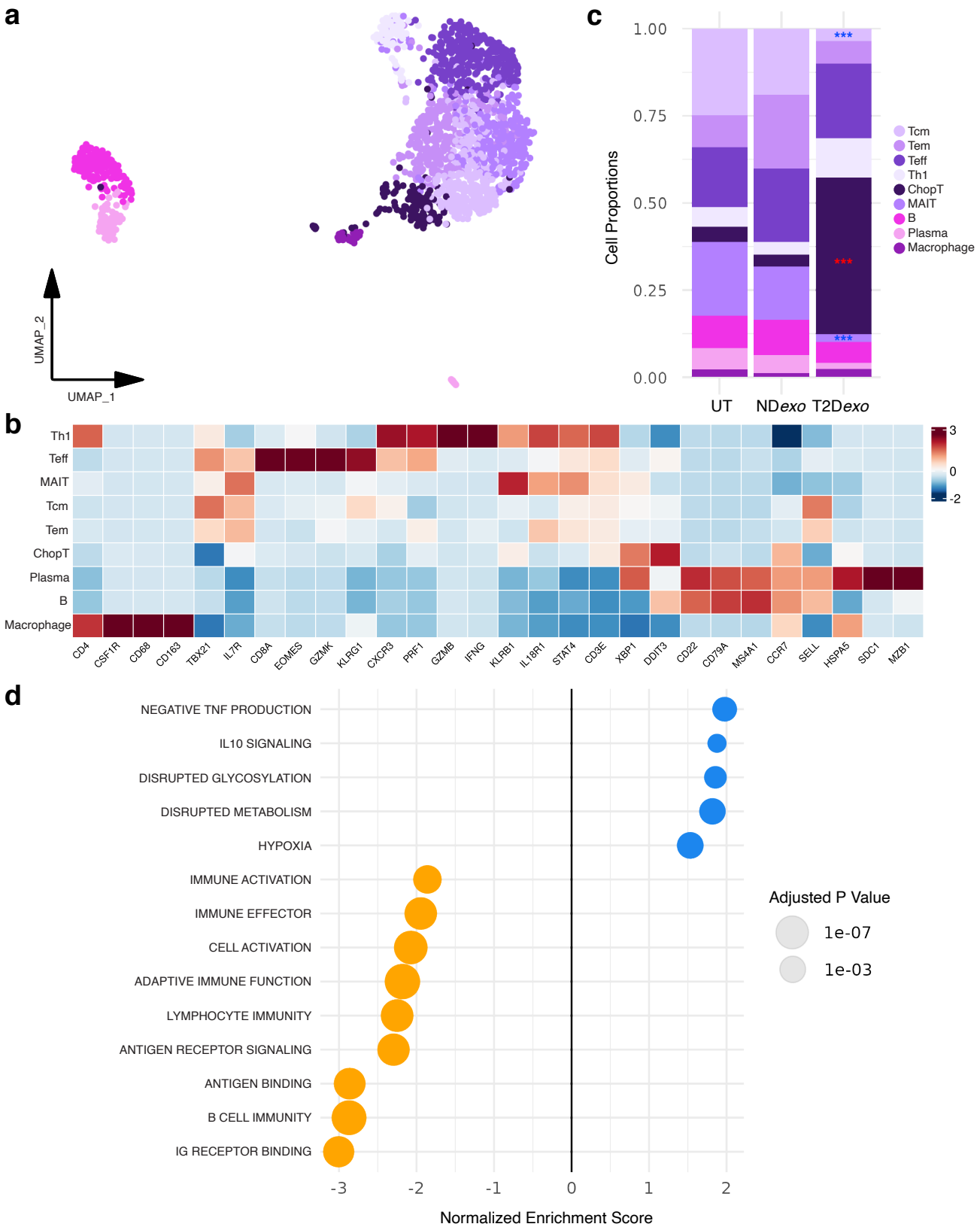
a
UMAP_2
UMAP_1
c
Cell Proportions
1.00
0.75
0.50
0.25
0.00
***
UT
NDexo
T2Dexo
Tcm
Tem
Teff
Th1
ChopT
MAIT
B
Plasma
Macrophage
b
Th1
Teff
MAIT
Tcm
Tem
ChopT
Plasma
B
Macrophage
CD4
CSF1R
CD68
CD163
TBX21
IL7R
CD8A
EOMES
GZMK
KLRG1
CXCR3
PRF1
GZMB
IFNG
KLRB1
IL18R1
STAT4
CD3E
XBP1
DDIT3
CD22
CD79A
MS4A1
CCR7
SELL
HSPA5
SDC1
MZB1
3
0
-2
d
NEGATIVE TNF PRODUCTION
IL10 SIGNALING
DISRUPTED GLYCOSYLATION
DISRUPTED METABOLISM
HYPOXIA
IMMUNE ACTIVATION
IMMUNE EFFECTOR
CELL ACTIVATION
ADAPTIVE IMMUNE FUNCTION
LYMPHOCYTE IMMUNITY
ANTIGEN RECEPTOR SIGNALING
ANTIGEN BINDING
B CELL IMMUNITY
IG RECEPTOR BINDING
-3
-2
-1
0
1
2
Normalized Enrichment Score
Adjusted P Value
1e-07
1e-03

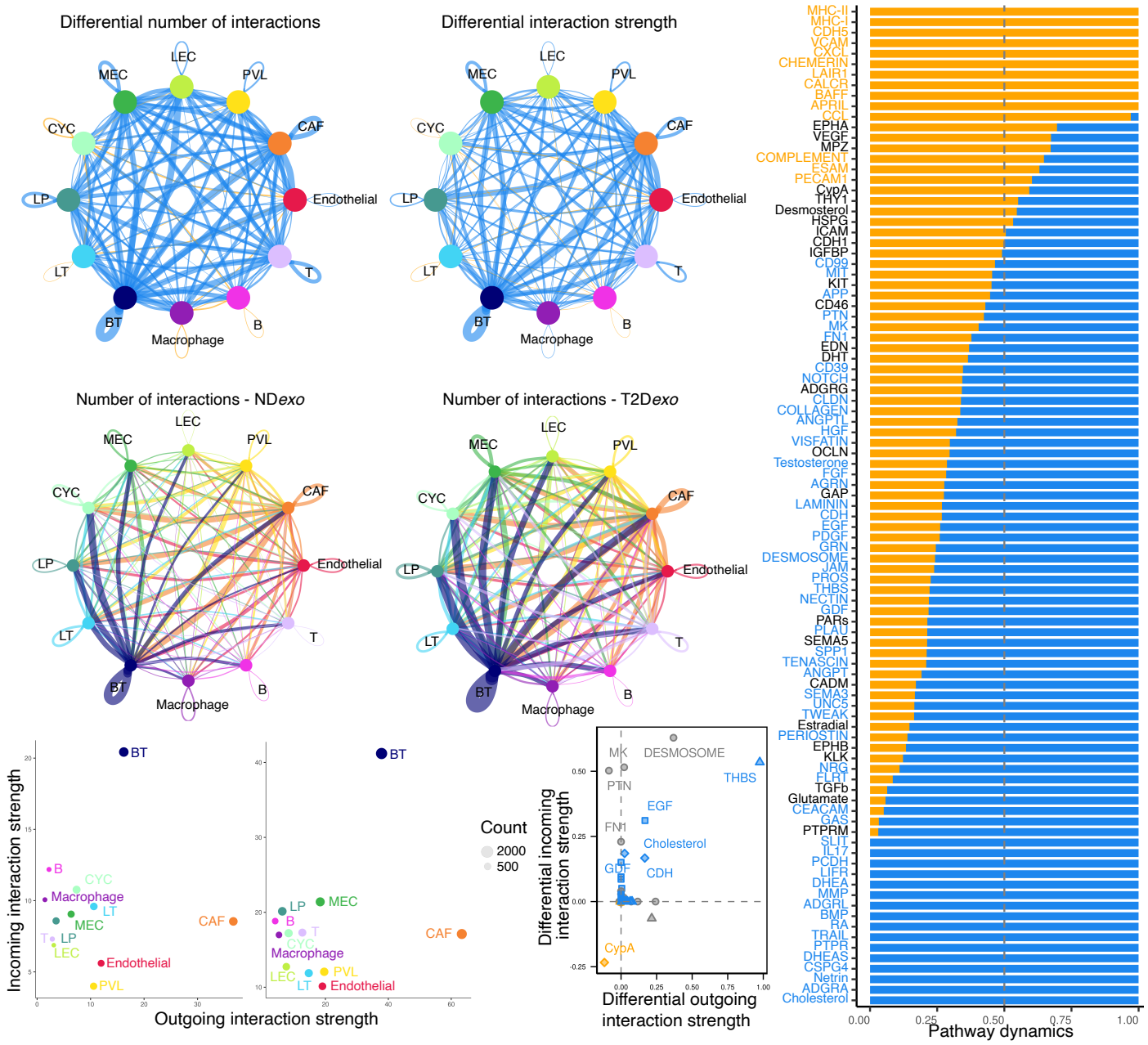
Differential number of interactions
Differential interaction strength
Number of interactions - ND*exo*
Number of interactions - T2D*exo*
LEC
PVL
CAF
Endothelial
T
B
Macrophage
BT
LT
LP
CYC
MEC
Incoming interaction strength
Outgoing interaction strength
Count
2000
500
Differential incoming interaction strength
Differential outgoing interaction strength
DESMOSOME
THBS
EGF
Cholesterol
CDH
MK
PTN
FN1
GDF
CypA
Pathway dynamics
MHC-II
MHC-I
CDH5
VCAM
CXCL
CHEMERIN
LAIR1
CALCR
BAFF
APRIL
CCL
EPHA
VEGF
MPZ
COMPLEMENT
ESAM
PECAM1
CypA
THY1
Desmosterol
HSPG
ICAM
CDH1
IGFBP
CD99
MIF
KIT
APP
CD46
PTN
MK
FN1
EDN
DHT
CD39
NOTCH
ADGRG
CLDN
COLLAGEN
ANGPTL
HGF
VISFATIN
OCLN
Testosterone
FGF
AGRN
GAP
LAMININ
CDH
EGF
PDGF
GRN
DESMOSOME
JAM
PROS
THBS
NECTIN
GDF
PARs
PLAU
SEMA5
SPP1
TENASCIN
ANGPT
CADM
SEMA3
UNC5
TWEAK
Estradial
PERIOSTIN
EPHB
KLK
NRG
FLRT
TGFb
Glutamate
CEACAM
GAS
PTPRM
SLIT
IL17
PCDH
LIFR
DHEA
MMP
ADGRL
BMP
RA
TRAIL
PTPR
DHEAS
CSPG4
Netrin
ADGRA
Cholesterol